

On a critical acceleration scale of dark matter in Λ CDM and dynamical dark energy

Zhijie (Jay) Xu,^{1*}

¹*Physical and Computational Sciences Directorate, Pacific Northwest National Laboratory; Richland, WA 99354, USA*

Accepted XXX. Received YYY; in original form ZZZ

ABSTRACT

Universal acceleration a_0 emerges in various empirical laws, yet its fundamental nature remains unclear. Using Illustris and Virgo N-body simulations, we focus on the velocity and acceleration fluctuations in collisionless dark matter involving long-range gravity. In contrast, in the kinetic theory of gases, molecules undergo random elastic collisions involving short-range interactions, where only velocity fluctuations are relevant. Hierarchical structure formation proceeds through the merging of smaller haloes to form larger haloes, which facilitates a continuous energy cascade from small to large haloes at a constant rate $\varepsilon_u \approx -10^{-7} \text{m}^2/\text{s}^3$. Velocity fluctuations involve a critical velocity $u_c \propto (1+z)^{-3/4}$. Acceleration fluctuations involve a critical acceleration $a_c \propto (1+z)^{3/4}$. Two critical quantities are related by the rate of energy cascade $\varepsilon_u \approx -a_c u_c / [2(3\pi)^2]$, where factor 3π is from the angle of incidence during merging. With critical velocity u_c on the order of 300 km/s at $z=0$, the critical acceleration is determined to be $a_{c0} \equiv a_c(z=0) \approx 10^{-10} \text{m/s}^2$, suggesting a_c might explain the universal acceleration $a_0 \approx 10^{-10} \text{m/s}^2$ in the empirical Tully-Fisher relation or modified Newtonian dynamics (MOND). The redshift evolution $a_c \propto (1+z)^{3/4}$ is in good agreement with Magneticum and EAGLE simulations and in reasonable agreement with limited observations. This suggests a larger a_0 at a higher redshift such that galaxies of fixed mass rotate faster at a higher redshift. Note that dark energy (DE) density $\rho_{DE0} \approx a_{c0}^2/G = 10^{-10} \text{J/m}^3$, we postulate an entropic origin of the dark energy from acceleration fluctuations of dark matter, in analogy to the gas pressure from velocity fluctuations. This leads to a dynamical dark energy coupled to the structure evolution involving a relatively constant DE density followed by a slow weakening phase, suggesting possible deviations from the standard Λ CDM paradigm.

Key words: Dark matter; Tully-Fisher; Galaxy rotation; MOND; Dark energy;

CONTENTS

- 1 Introduction
- 2 Distributions of dark matter acceleration
- 3 Distributions of dark matter velocity
- 4 The energy cascade in dark matter
- 5 The critical acceleration a_c from energy cascade
- 6 Simulations and observations for redshift evolution of a_c
- 7 The origin of universal acceleration a_0
- 8 Relevant physical quantities on small and large scales
- 9 Dark energy from acceleration fluctuations
- 10 Conclusions

1 INTRODUCTION

The dark matter problem originates from the mass discrepancy between the amount of dynamical mass required by the motions of astronomical objects and the directly observed luminous mass. The flat rotation curves of spiral galaxies directly point to that mass discrepancy problem: the total mass predicted by Newtonian gravity is much greater than the observed luminous mass [1, 2]. The standard cosmological model (Λ CDM) interprets this mass discrepancy

in terms of cold dark matter (CDM) [3, 4, 5] that is believed to be cold (non-relativistic), collisionless, dissipationless, non-baryonic, and interacts with baryonic matter only through gravity. The Λ CDM model has been highly successful in the formation and evolution of large-scale structures, the cosmic microwave background, the distribution of galaxies, and the matter content of the universe [3, 4, 5, 6]. However, the theory also encounters several difficulties on small scales [7, 8, 9] in describing small-scale structures, including the "cusp/core" problem [10, 11, 12], the "missing satellite" problem [13, 14, 15, 16], and the problem of re-obtaining the baryonic Tully-Fisher relation [8].

The original Tully-Fisher relation was proposed to empirically correlate the rotation velocity v_f of a spiral galaxy with its intrinsic luminosity or stellar mass [17]. A similar scaling was also observed for the dispersion of the random velocity of stars [18]. The Tully-Fisher relation has been generalized to using the total baryonic mass M_b instead of just the stellar mass. The resulting baryonic Tully-Fisher relation (BTFR) is a well-established empirical relation between the total baryonic mass M_b (stellar plus gas) and the flat rotation velocity v_f that extends for six decades in M_b [19, 20, 21]. In BTFR, the scaling $v_f \propto M_b^{1/4}$ between the rotation velocity v_f and the baryonic mass M_b [22] can be written as

$$v_f^4 = GM_b a_0, \quad (1)$$

* E-mail: zhijie.xu@pnnl.gov; zhijieXu@hotmail.com

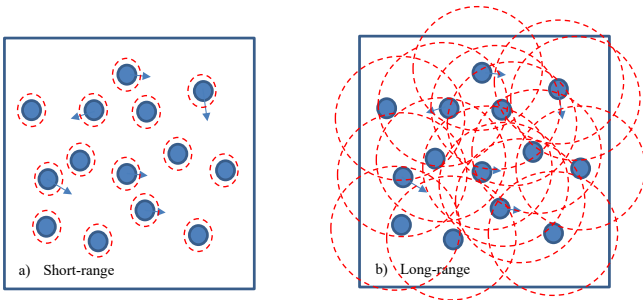


Figure 1. The Schematic plot of systems that involve short-range and long-range interactions (red dashed line for interaction range): a) In the kinetic theory of gases, molecules undergo random elastic collisions that involve only short-range interactions. Molecules interact only with other molecules within a very short distance. For a dilute system, most of the molecules are out of the interaction range of other molecules. Therefore, only velocity fluctuations are relevant, which usually follows a Boltzmann distribution (Eq. (5)); b) For self-gravitating dark matter, particles interact with all other particles through long-range gravity such that a small change in any particle position leads to perturbations in accelerations of all other particles. Therefore, both velocity fluctuations and acceleration fluctuations are relevant for self-gravitating dark matter and are discussed in detail in this paper (Fig. 3 and Eq. (7)).

where G is the gravitational constant and $a_0 \approx 10^{-10} \text{m/s}^2$ is an empirical constant of acceleration.

One problem in understanding the BTFR lies in the discrepancy between the scatter and the slope inferred from the model and those from observations [23]. Furthermore, the BTFR obtained from Λ CDM simulations also shows a larger scatter than that of observations [23]. Some recent simulations that account for stellar feedback processes have shown improved agreement. However, it remains challenging to understand the scaling and scatter of the Tully-Fisher relation [8, 24], as well as the origin of empirical acceleration a_0 .

Beyond the Λ CDM cosmology, an alternative interpretation resorts to the modification of gravity that might eliminate the need for dark matter for the mass discrepancy problem. The modified Newtonian dynamics (MOND) is an empirical model proposed to reproduce these astronomical observations without invoking the dark matter hypothesis [25]. The basic idea of MOND is to introduce a universal acceleration scale $a_0 \approx 1.2 \times 10^{-10} \text{m/s}^2$. Standard Newtonian mechanics $F = ma$ is recovered when acceleration $a \gg a_0$. For the so-called "deep-MOND" regime with $a \ll a_0$, Newtonian mechanics needs to be modified to $F = ma^2/a_0$, that is, the external force $F \propto a^2$. Section 7 provides more details on this ad hoc theory. MOND might explain the shape of the rotation curves [26], the baryonic Tully-Fisher relation [19, 27], and the tight correlation between the radial acceleration of the rotation curves and that of the observed baryons [28]. However, recent studies also suggest that Λ CDM is also consistent with the radial acceleration relation [29]. This motivates the search for a theory for the observed scaling ($v_f \propto M_b^{1/4}$) and the origin of the empirical acceleration a_0 within the Λ CDM paradigm.

Small-scale challenges to Λ CDM strongly indicate missing pieces in our understanding of dark matter physics. In this paper, we discuss the acceleration fluctuations in dark matter and identify a fluctuation-induced critical acceleration a_c that might explain the empirical acceleration a_0 in BTFR. The existence of velocity fluctuations in dark matter is well known, where the probability distributions of dark matter velocity have been extensively studied [30, 31, 32, 33, 34]. This paper focuses on the acceleration fluctuations in dark matter and their effects on the dynamics of galaxies and dark matter haloes. Potential connections between acceleration fluctuations and dark energy were

also proposed in analogy to the connections between pressure and velocity fluctuations.

As shown in Fig. 1 b), due to the long-range nature of gravity, every dark matter particle interacts with all other particles such that a small change in any particle position leads to perturbations in the acceleration of all other particles. This leads to fluctuations in particle acceleration and a redshift-dependent probability distribution of particle accelerations. On the contrary, in the kinetic theory of gases in Fig. 1 a), molecules undergo random elastic collisions that involve short-range interactions. Molecules interact only with other molecules within a very short distance. Changes in any molecule's position do not lead to perturbations in the acceleration of other molecules. Therefore, only velocity fluctuations are relevant for systems involving short-range interactions.

Compared to the velocity distributions and correlations that have been extensively studied [32, 33, 34, 35], more work is required to understand the nature of acceleration fluctuations and distributions on different length and time scales. The existence of acceleration fluctuations naturally leads to a critical acceleration scale a_c , the root mean square (RMS) acceleration, for a given distribution of particle accelerations. In this paper, we will focus on the acceleration fluctuations, the critical acceleration a_c , its relation to empirical acceleration a_0 in BTFR, and potential connections to dark energy. The remainder of the paper is organized as follows. Section 2 presents the redshift evolution of the acceleration distributions from the N-body simulations, followed by the velocity distributions in Section 3. The velocity and acceleration fluctuations are closely related to each other, connected by an energy cascade process during the hierarchical structure formation (Sections 4 and 5). Section 6 presents the simulations and observations for the redshift variation of a_0 . The connection with empirical MOND acceleration a_0 is presented in Section 7, along with a theory for "Non-Newtonian" behavior at small acceleration ($a \ll a_0$). Section 8 presents relevant physical quantities based on fluctuations in dark matter, followed by Section 9 on potential connections to dark energy.

2 DISTRIBUTIONS OF DARK MATTER ACCELERATION

In this section, we focus on the acceleration distributions of dark matter particles from N-body simulations. The basic dynamics of the self-gravitating collisionless dark matter flow (SG-CFD) is governed by collisionless Boltzmann equations (CBE) [36] that can be numerically solved by particle-based N-body simulations [37]. As a first step, we focus on the dark matter only simulations. The simulation data were generated from the large-scale N-body simulations by the Virgo consortium or the SCDM model (the matter-dominant cold dark matter model) with $\Omega_{DM} = 1$. This suite of cosmological simulations is a dark matter only with a 240Mpc^3 volume. Each dark matter particle has a mass around $m_p = 4.54 \times 10^{11} M_\odot$. The gravitational softening length is around 36 kpc. More details can be found in [38]. The same set of simulation data has also been widely used to study clustering statistics [39], the formation of halo clusters [40], and to test halo mass functions [41].

In this paper, to cross-check some results, we also use the Illustris simulations (Illustris-1-Dark for dark matter only), a more recent suite of cosmological simulations with a much higher mass resolution of $m_p = 7.6 \times 10^6 M_\odot$ [42]. The simulation has cosmological parameters of dark matter density $\Omega_{DM} = 0.2726$, dark energy density $\Omega_{DE} = 0.7274$ at $z = 0$, and Hubble constant $h = 0.704$. The simulation results of the Illustris simulations will be explicitly indicated in the figures.

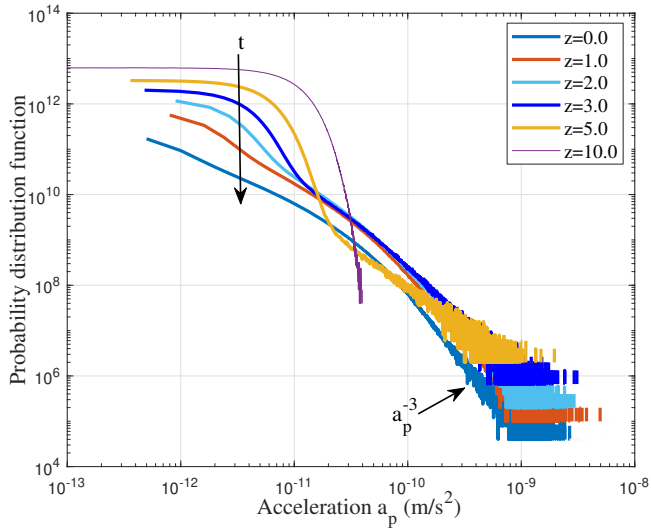


Figure 2. The redshift evolution of the probability distribution of particle acceleration a_p for all particles in an N-body system (SCDM). A long tail $\propto a_p^{-3}$ is gradually formed from $z=5$ due to the formation of halo structures.

For both simulations, the Friends of Friends (FOF) algorithm was used to identify all haloes in the simulation that depend only on a dimensionless parameter b , which defines the linking length $b(N/V)^{-1/3}$. Here, N is the number of total particles, and V is the volume of the simulation box. All haloes in the simulation were identified with a linking length parameter $b = 0.2$. After identifying all haloes in the N-body system, all dark matter particles can be divided into two groups: halo particles ("hp") and out-of-halo particles ("op", particles that do not belong to any haloes). This is important because the velocity and acceleration statistics of particles in two groups are very different and should be studied separately.

By calculating the total force for every dark matter particle, the proper acceleration \mathbf{a}_p for particle i is

$$\mathbf{a}_p = \frac{Gm_p}{a^2} \sum_{j \neq i}^N \frac{\mathbf{x}_i - \mathbf{x}_j}{|\mathbf{x}_i - \mathbf{x}_j|^3}, \quad (2)$$

where \mathbf{x}_i and \mathbf{x}_j are the comoving coordinates of particles i and j . The summation runs over all other particles except i . The periodic boundary is also taken care of in the calculation, with a total of 26 replicas of the simulation domain in three dimensions to approximate the long-range gravity.

Figure 2 plots the redshift variation of the acceleration distribution, i.e., the distribution of Cartesian components $[a_{px}, a_{py}, a_{pz}]$ of the acceleration vector \mathbf{a}_p for all dark matter particles. Particle acceleration evolves from an initial Gaussian distribution at high redshift to a distribution with a long tail $\propto a_p^{-3}$ for large acceleration in the halo core region. The tail starts to form at around $z=5$ due to the formation and evolution of halo structures.

By dividing all particles into halo and out-of-halo particles, Fig. 3 plots the evolution of the acceleration distribution for halo particles (a_{hp} : solid lines) and for out-of-halo particles (a_{op} : dashed lines), respectively. The long tail $\propto a_{hp}^{-3}$ at large acceleration comes from the halo core region with a higher dark matter density. The maximum acceleration is determined by the highest density in the halo core and seems independent of the redshift. With continuous mass accretion, more particles are accreted into the halo outskirts, and the distribution gradually extends to smaller acceleration. The distribution of a_{op} for out-of-halo particles is approximately Gaussian at high redshift.

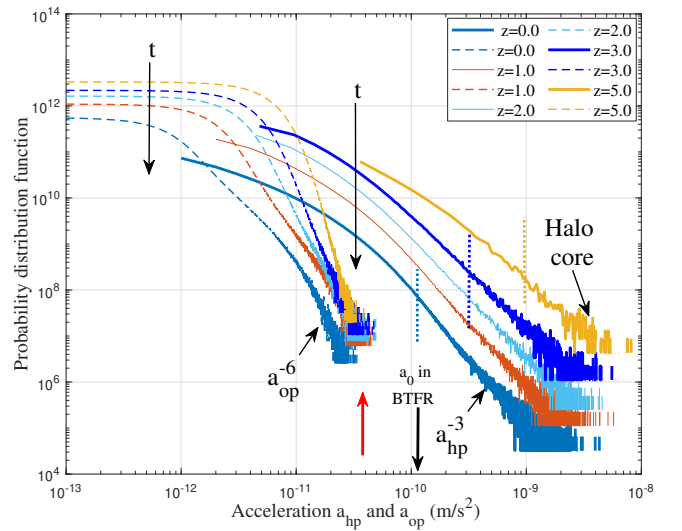


Figure 3. The redshift evolution of the probability distributions of halo particle acceleration a_{hp} (solid lines) and out-of-halo particle acceleration a_{op} (dashed lines). A long tail $\propto a_{hp}^{-3}$ at large acceleration is a typical feature due to halo particles in the core region. The distribution of a_{op} for out-of-halo particles is approximately Gaussian at high redshift. For both types of particles, the acceleration decreases with time because of expanding space. The dotted lines represent the standard deviation of the acceleration distribution (RMS acceleration) at $z = 5, 3$, and 0 . The time variation of the RMS acceleration is presented in Fig. 4. The empirical BTFR acceleration ($a_0 \approx 10^{-10} \text{ m/s}^2$) is marked on the graph (black arrow) that matches the RMS acceleration of the N-body simulation at $z = 0$. This is not just a coincidence but suggests a fluctuation origin of the empirical acceleration a_0 in BTFR (Section 7).

Acceleration decreases with time due to expanding space (also see Fig. 4). The out-of-halo particles with the largest acceleration should be those particles close to the haloes with which they are going to merge (red arrow). The dotted lines represent the standard deviation of the acceleration distribution (the root mean square acceleration or RMS) at $z = 5, 3$, and 0 . The empirical BTFR acceleration a_0 is marked by the black arrow that matches the RMS acceleration at $z = 0$ (blue dotted line). This is not a coincidence. We will show that the RMS acceleration, i.e. the scale of acceleration fluctuation, is related to a_0 in Section 7.

To better describe the distribution and evolution of acceleration and velocity, we start by decomposing the particle acceleration and velocity into two parts of different natures. In N-body simulations, every halo particle ("hp"), characterized by a mass, m_p , a velocity vector, \mathbf{v}_{hp} , and an acceleration vector \mathbf{a}_{hp} , should belong to one and only one particular parent halo. For each identified halo, the total acceleration \mathbf{a}_{hp} and velocity \mathbf{v}_{hp} of each halo particle can be decomposed into mean values and fluctuations around these mean values [32]. These mean values are the halo acceleration and halo velocity, respectively,

$$\mathbf{a}_h = \langle \mathbf{a}_{hp} \rangle_h = \frac{1}{n_p} \sum_{k=1}^{n_p} \mathbf{a}_{hp}, \quad \mathbf{v}_h = \langle \mathbf{v}_{hp} \rangle_h = \frac{1}{n_p} \sum_{k=1}^{n_p} \mathbf{v}_{hp}, \quad (3)$$

where $\langle \cdot \rangle_h$ stands for the average of a quantity over all n_p particles in a given halo. These mean values are related to the inter-halo interactions between any particle and all other particles outside the halo in which the particle resides. The inter-halo interactions are weaker, operating on larger scales and in the linear regime [43].

On the other hand, fluctuations in acceleration and velocity of halo

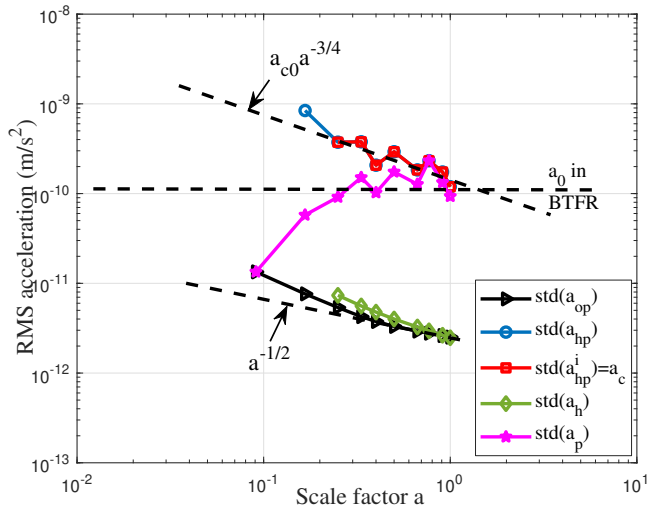


Figure 4. The variation of RMS accelerations (m/s^2) with scale factor a for all particles (a_p : magenta), halo particles (a_{hp} : blue), out-of-halo particles (a_{op} : black), haloes (a_h : green), and acceleration fluctuation of all halo particles (a_{hp}^i : red). All accelerations decrease with time except the RMS acceleration for all particles a_p . The halo acceleration a_h matches the acceleration of the out-of-halo particles a_{op} and is much smaller ($\sim 10^{-12} \text{m/s}^2$) due to weaker gravity on large scales. The acceleration of the halo particles a_{hp} can be decomposed into the halo acceleration a_h and the fluctuation a_{hp}^i (Eq. (4)). Here, $\text{std}(a_h) \propto a^{-1/2}$ evolves in the linear regime, and the critical acceleration scale $a_c = \text{std}(a_{hp}^i) \propto a^{-3/4}$ evolves in the nonlinear regime (Eq. (25)). At $z=0$, the critical acceleration of fluctuation (a_c) matches the empirical acceleration $a_0 = 10^{-10} \text{m/s}^2$, suggesting the connection between the critical acceleration a_c and the empirical acceleration a_0 in the baryonic Tully-Fisher relation (BTFR in Section 7). The RMS acceleration for all particles a_p is approximately a weighted average of out-of-halo particle acceleration a_{op} and halo particle acceleration a_{hp} (Eq. (40)). It does increase with time due to the increasing number of halo particles from halo structure formation and evolution.

particles are defined as

$$\begin{aligned} \mathbf{a}_{hp}^i &= \mathbf{a}_{hp} - \langle \mathbf{a}_{hp} \rangle_h = \mathbf{a}_{hp} - \mathbf{a}_h, \\ \mathbf{v}_{hp}^i &= \mathbf{v}_{hp} - \langle \mathbf{v}_{hp} \rangle_h = \mathbf{v}_{hp} - \mathbf{v}_h, \end{aligned} \quad (4)$$

where acceleration fluctuation \mathbf{a}_{hp}^i and velocity fluctuation \mathbf{v}_{hp}^i are related to the intra-halo interactions between that particle and all other particles in the same halo. In contrast, the intra-halo interactions are stronger, operating on smaller scales and in the nonlinear regime [43, 44].

Due to the different nature of inter- and intra-halo interactions, the halo velocity and acceleration (\mathbf{v}_h and \mathbf{a}_h) evolve in the linear regime, whereas the velocity and acceleration fluctuations (\mathbf{v}_{hp}^i and \mathbf{a}_{hp}^i) evolve in the nonlinear regime (see Figs. 4 and 5). In this paper, the mean velocity \mathbf{v}_h and acceleration \mathbf{a}_h refer to the mean velocity and acceleration of all particles in the same halo, i.e., the velocity and acceleration of that halo (Eq. (3)). Fluctuations (\mathbf{v}_{hp}^i and \mathbf{a}_{hp}^i) refer to the velocity and acceleration of halo particles that fluctuate around their mean values \mathbf{v}_h and \mathbf{a}_h (Eq. (4)).

Figure 4 plots the time variation of the RMS acceleration ($\sqrt{3} \times$ standard deviation of the distributions in Fig. 3), that is, the root mean square acceleration for halo particles (blue), out-of-halo particles (black), haloes (green), and acceleration fluctuations (red), where the factor $\sqrt{3}$ is for the magnitude of the acceleration vector in a 3D space. Halo acceleration a_h is the mean acceleration of all particles in

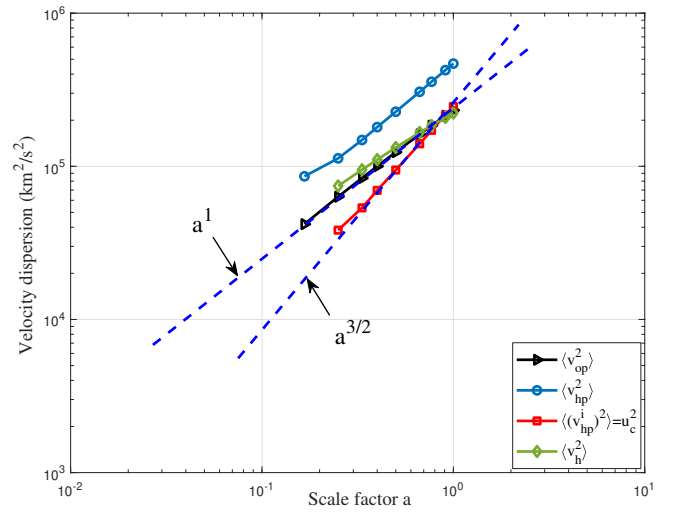


Figure 5. The variation of velocity dispersions (km^2/s^2) with scale factor a for halo particles (v_{hp} : blue), out-of-halo particles (v_{op} : black), haloes (v_h : green), and velocity fluctuation of halo particles (v_{hp}^i : red). All velocity dispersions increase with time. The dispersion of halo velocity v_h matches the out-of-halo particle velocity v_{op} . The velocity of halo particles v_{hp} can be decomposed into the halo velocity v_h and the fluctuation v_{hp}^i (Eq. (4)). Here, the dispersion of halo velocity v_h evolves as $\propto a \propto t^{2/3}$ (in the linear regime due to inter-halo interaction on large scales). The dispersion of velocity fluctuation v_{hp}^i (or the critical velocity scale u_c^2) evolves as $\propto a^{3/2} \propto t$ (in the nonlinear regime due to intra-halo interaction on small scales).

the same halo (Eq. (3)). All RMS accelerations decrease with time but evolve differently. The standard deviation of the halo acceleration a_h and the out-of-halo particle acceleration a_{op} evolves as $\propto a^{-1/2} \propto t^{-1/3}$ (the linear regime due to inter-halo interactions on large scales). The standard deviation of acceleration fluctuations $a_c = \text{std}(a_{hp}^i)$ evolves approximately as $a_c \propto a^{-3/4} \propto t^{-1/2}$ in the nonlinear regime due to intra-halo interactions on small scales. The RMS acceleration for all particles a_p can be approximated as a weighted average of out-of-halo particle acceleration a_{op} and halo particle acceleration a_{hp} (Eq. (40)). It does increase with time due to the increasing number of halo particles.

On large scales, haloes and out-of-halo particles have similar accelerations that are much smaller than the acceleration of halo particles due to the large distance between different haloes and between out-of-halo particles ($\approx 10^{-12} \text{m/s}^2$, green and black lines). At $z=0$, the critical acceleration of fluctuations a_c matches the empirical acceleration of BTFR $a_0 \approx 10^{-10} \text{m/s}^2$. This suggests a potential relationship between the critical acceleration a_c (the RMS of acceleration fluctuations) and the empirical acceleration a_0 .

Similarly, Figure 5 plots the time variation of the velocity variance (or specific kinetic energy). The halo velocity v_h is the mean velocity of all particles in the same halo (Eq. (3)). The dispersion of the halo velocity v_h matches the dispersion of the out-of-halo particle velocity v_{op} . Both velocity dispersions have a linear scaling $\propto a$ that manifests the linear regime on large scales. Therefore, haloes behave like macro-particles on large scales with an evolution of acceleration and velocity similar to that of out-of-halo particles (see Figs. 4 and 5). The velocity dispersions of haloes and out-of-halo particles evolve as $(\propto a \propto t^{2/3})$ due to inter-halo interactions on large scales that are in the linear regime. The dispersion of velocity fluctuations evolves as $\propto a^{3/2} \propto t$ due to the intra-halo interactions on small scales in the nonlinear regime.

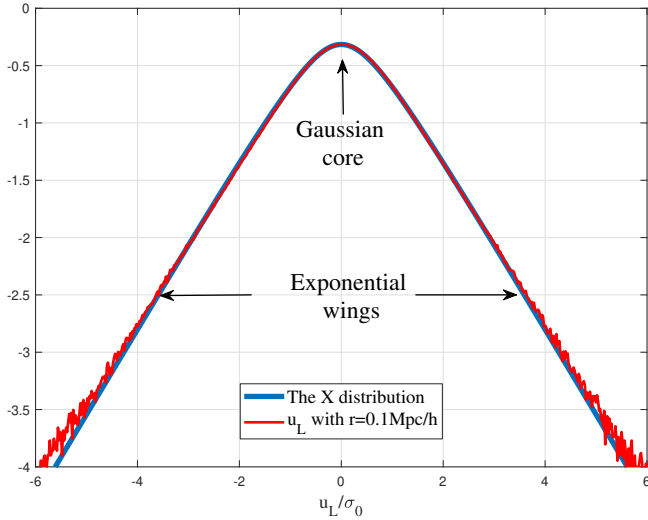


Figure 6. The X distribution with a unit variance compared with the velocity distribution from N -body simulation (u_L normalized by σ_0). The vertical axis is in the logarithmic scale (\log_{10}). The X distribution with $\alpha = 1.33$ and $v_0^2 = 1/3\sigma_0^2$ matches the velocity distribution on a small scale r , where all pairs of particles are likely from the same halo. The Gaussian core ($u_L < v_0$) and exponential wings ($u_L > v_0$) can be clearly identified.

3 DISTRIBUTIONS OF DARK MATTER VELOCITY

Since acceleration and velocity fluctuations are tightly connected in the self-gravitating collisionless dark matter, this section focuses on the velocity distribution in dark matter, which is also required to understand the origin of empirical acceleration a_0 in Section 7.

The velocity distributions of dark matter particles can be studied by N -body simulations and by the theory of maximum entropy [32]. The principle of maximum entropy requires a velocity distribution with the highest entropy and the least prior information [45, 46]. In the kinetic theory of gases, the maximum entropy distribution of the molecule's velocity follows the well-known Boltzmann statistics,

$$f(v) = \frac{1}{\sqrt{2\pi}v_0} \exp\left(-\frac{v^2}{2v_0^2}\right), \quad (5)$$

where v_0^2 is the dispersion or the scale of velocity fluctuation. The Maxwell-Boltzmann distribution of particle speed reads

$$Z(v) = -2v \frac{\partial f}{\partial v} = \sqrt{\frac{2}{\pi}} \frac{v^2}{v_0^3} \exp\left(-\frac{v^2}{2v_0^2}\right). \quad (6)$$

For systems involving short-range interactions, the maximum entropy distribution of the velocity is Gaussian (Eq. (5)).

For self-gravitating collisionless dark matter involving long-range gravity, the maximum entropy distribution of particle velocity (denoted as the X) can also be analytically derived [32]. This can be achieved by applying the virial theorem for mechanical equilibrium and the maximum entropy principle for statistical equilibrium. Here, we briefly present the main results. The maximum entropy distribution of particle velocity (X distribution) reads [32]

$$X(v) = \frac{1}{2\alpha v_0} \frac{e^{-\sqrt{\alpha^2 + (v/v_0)^2}}}{K_1(\alpha)}, \quad (7)$$

where $K_y(x)$ is a modified Bessel function of the *second kind*. Similarly to Eq. (5), v_0 is a velocity scale (the scale of velocity fluctuation). Here, α is a shape parameter that dominates the shape of X

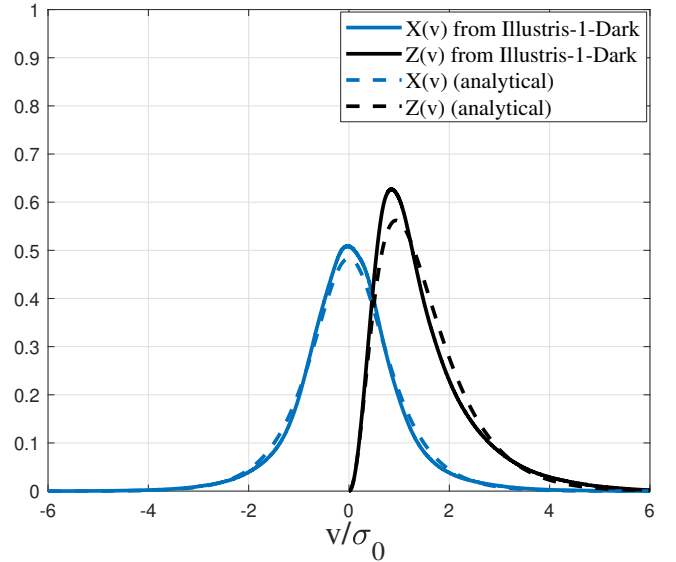


Figure 7. The X distribution for particle velocity and Z distribution for particle speed from Illustris-1-dark simulation. Velocity is normalized by the standard deviation σ_0 in Eq. (8). The shape parameter $\alpha = 1.33$ and the velocity scale $v_0^2 = 1/3\sigma_0^2$. Dashed lines present the analytical model of velocity and speed distributions from Eqs. (7) and (9).

distribution. The X distribution approaches a double-sided Laplace (exponential) distribution with $\alpha \rightarrow 0$ and a Gaussian distribution with $\alpha \rightarrow \infty$, respectively. The second-order moment (variance) of the X distribution reads:

$$\text{Var}(v) = \alpha \frac{K_2(\alpha)}{K_1(\alpha)} v_0^2 = \sigma_0^2. \quad (8)$$

Similarly to the Maxwell-Boltzmann distribution in Eq. (6), the distribution of particle speed $Z(v)$ reads

$$Z(v) = -2v \frac{\partial X}{\partial v} = \frac{1}{\alpha K_1(\alpha)} \cdot \frac{v^2}{v_0^3} \cdot \frac{e^{-\sqrt{\alpha^2 + (v/v_0)^2}}}{\sqrt{\alpha^2 + (v/v_0)^2}}. \quad (9)$$

Figure 6 presents the comparison of X distribution with the N -body simulation (SCDM). For all pairs of particles with a given separation r , the longitudinal velocity u_L is calculated as the projection of the particle velocity \mathbf{u} along the vector of separation \mathbf{r} , that is, $u_L = \mathbf{u} \cdot \mathbf{r}$. In this graph, the parameters $\alpha = 1.33$, $v_0^2 = 1/3\sigma_0^2$ (from Eq. (8)), and the velocity variance $\sigma_0^2 = \text{var}(u_L)$ for all pairs of particles on a small scale of $r \equiv |\mathbf{r}| = 0.1 \text{ Mpc}/h$ at $z = 0$ [32, 34]. For intermediate $\alpha \sim 1$, the X distribution naturally exhibits a Gaussian core at low velocity $v \ll v_0$ and exponential wings at high velocity $v \gg v_0$, as shown in Fig. 6. Here, we find v_0 , the scale of velocity fluctuation, that delineates two regimes. In this case, the X distribution in Eq. (7) can be expressed separately, that is, the Gaussian core for small velocity and the exponential wings for large velocity:

$$X(v) = \frac{e^{-\alpha}}{2\alpha v_0 K_1(\alpha)} \exp\left(-\frac{v^2}{2\alpha v_0^2}\right) \quad \text{for } |v| \ll v_0, \quad (10)$$

$$X(v) = \frac{1}{2\alpha v_0 K_1(\alpha)} \exp\left(-\frac{v}{v_0}\right) \quad \text{for } |v| \gg v_0.$$

This is also consistent with other N -body simulation results [47].

Figure 7 presents a similar comparison with the Illustris-1-Dark simulation [42]. We first identify all haloes and halo particles. Solid lines present the velocity and speed distributions of all halo particles,

while dashed lines plot the X and Z distributions from Eqs. (7) and (9). Compared to the better agreement in Fig. 6, the small discrepancy in Fig. 7 reflects the fact that some haloes may not be fully virialized.

Comparing the X distribution with the Gaussian distribution $f(v)$ in Eq. (5), the effect of long-range gravity on velocity distributions can be clearly demonstrated. For a small velocity $v \ll v_0$ of particles in the halo core region or small virialized haloes, the distribution is approximately Gaussian. For dark matter particles in the outer region of the haloes with a high velocity $v \gg v_0$, the velocity distribution deviates from Gaussian and approaches an exponential distribution, reflecting the effect of long-range inter-halo gravity on particles with high velocity.

Next, let us look at the specific kinetic energy of dark matter particles (energy per unit mass) that will provide more insight into the effect of long-range gravity. In Newtonian mechanics, the specific kinetic energy $\varepsilon_K(v) = v^2/2$. For self-gravitating collisionless dark matter, the specific kinetic energy $\varepsilon_K(v)$ for all particles with a given speed v can be obtained from the maximum entropy distribution [32],

$$\varepsilon_K(v) = -\frac{3}{2} \frac{X(v)v^2}{v \partial X / \partial v} = \frac{3X(v)v^2}{Z(v)}, \quad (11)$$

where $X(v)v^2 dv$ is the total kinetic energy for all particles with a given speed v , while $v \partial X / \partial v dv$ is the total number of particles with that given speed v (e.g. Eq. (9)). Substitution of Eqs. (7) and (9) into Eq. (11) leads to the effective kinetic energy (Specific) as a function of particle speed v ,

$$\varepsilon_K(v) = \frac{3}{2} v_0^2 \sqrt{\alpha^2 + \left(\frac{v}{v_0}\right)^2}. \quad (12)$$

Note that ε_K represents the effective kinetic energy.

In N-body simulation, we can identify all particles with a given speed v at any moment with instantaneous energy of $\varepsilon_i(v) = v^2/2 + \phi_i$, where ϕ_i is the potential energy of that particle at that moment. The average total energy of all particles with the same speed v can be written as

$$\langle \varepsilon_i(v) \rangle = \varepsilon_K + \varepsilon_P \quad \text{and} \quad 2\varepsilon_K = n\varepsilon_P, \quad (13)$$

where the effective kinetic energy ε_K and potential energy ε_P obey the virial theorem and n is the potential exponent. Particles with the same speed v can be in haloes of different sizes with different instantaneous potential ϕ_i . The virial theorem is valid in the sense of averaging over an ensemble of all particles with the same speed v or averaging over the time trajectory of a given particle. Therefore, the effective particle kinetic energy ε_K reflects the averaged particle kinetic energy for all particles with the same speed.

For self-gravitating dark matter, the particle kinetic energy $\varepsilon_K(v)$ has two regimes from Eq. (12) that follow a linear scaling and a parabolic scaling, respectively,

$$\varepsilon_K(v) \approx \frac{3}{2} v_0 v \quad \text{for} \quad v \gg v_0, \quad (14)$$

$$\varepsilon_K(v) \approx \underbrace{\frac{3}{2} \alpha v_0^2}_1 + \underbrace{\frac{3v^2}{4\alpha}}_2 \quad \text{for} \quad v \ll v_0.$$

For particles with a small velocity $v \ll v_0$, term 1 is the contribution from the halo velocity v_h , i.e., the mean velocity of all particles in the same halo. High-speed particles are usually in the outskirts of haloes with extremely small acceleration. Due to the long-range nature of gravity, their dynamics are dominated by both inter- and intra-halo interactions. The superposition of all intra- and inter-halo interactions leads to the linear scaling for kinetic energy $\varepsilon_K(v) \propto v_0 v$,

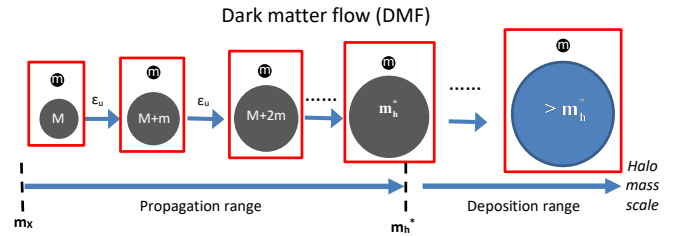


Figure 8. Schematic plot of the mass and energy cascade in dark matter flow. Hierarchical structure formation proceeds via halo merging to give rise to larger haloes. Haloes merge with smaller haloes to give rise to larger haloes and produce a continuous mass/energy flux to larger mass scales, that is, a continuous inverse mass and kinetic energy cascade in the halo mass space. While the potential energy is directly cascaded from large to small scales. Scale-independent rate of mass cascade (ε_m in Eq. (17)) and rate of (kinetic) energy cascade (ε_u in Eq. (21)) are expected in a certain range of mass scales (propagation range). The mass/energy cascaded from small scales is consumed to grow haloes on scales greater than m_h^* (deposition range). Figure 16 presents a typical two-body merging to calculate the rate of the energy cascade ε_u . Table 1 presents the relevant physical quantities on the smallest scale (m_x) and the largest scale (m_h^*) of the propagation range. More details can be found in previous work [43, 48, 49, 50] and the applications for universal halo density profile, halo mass function, and dark matter particle properties.

which emerges from the maximum entropy principle. This scaling can also be confirmed by N-body simulations [32]. On the contrary, the dynamics of low-speed particles in the halo core region are dominated only by the intra-halo interaction with Newtonian behavior, that is, $\varepsilon_K(v) \propto v^2$.

In summary, the velocity distributions of dark matter involve a typical velocity scale v_0 (the scale of fluctuation). Depending on the particle velocity v , the effective kinetic energy ε_K follows $\varepsilon_K(v) \propto v^2$ for low speed ($v \ll v_0$), that is, a standard Newtonian behavior. However, $\varepsilon_K(v) \propto v_0 v$ for high-speed ($v \gg v_0$) is a unique "non-Newtonian" feature due to long-range gravity in dark matter. These results will be used to explain the non-Newtonian behavior and the empirical MOND acceleration a_0 in Section 7.

4 THE ENERGY CASCADE IN DARK MATTER

The acceleration and velocity fluctuations are not independent of each other. In fact, two fluctuations are intrinsically connected through an energy cascade process in dark matter, which has been extensively discussed in previous work. Halo mass functions, density profiles, and universal scaling laws can be systematically derived based on the concept of energy cascade across haloes of different sizes [48, 49, 50], where the readers can find more details. Here, we provide a brief overview, as shown in Fig. 8, followed by illustrations of the concept from the results of N-body simulations.

First, long-range gravity requires the formation of different sizes of haloes to maximize the entropy of the system [32]. These localized overdense halo structures (building blocks in dark matter flow) facilitate the formation of hierarchical structures via halo merging to give rise to larger and larger structures (see Fig. 8). Due to hierarchical structure formation, haloes of mass M merge with a smaller halo of mass m to produce a mass/energy flux into the scale of $M+m$ in the halo mass space. Continuous halo structure merging facilitates a continuous mass/energy cascade (or flux) from small to large scales to form larger and larger structures. This halo-mediated cas-

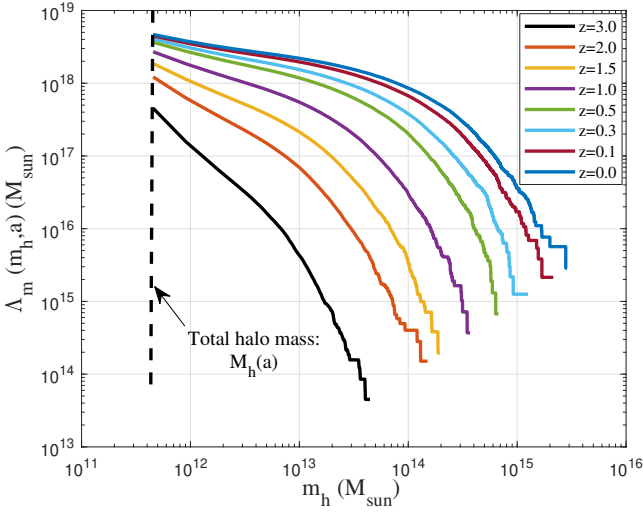


Figure 9. The variation of cumulative mass function $\Lambda_m(m_h, a)$ with halo mass scale m_h at different redshifts z . The total mass $M_h(a)$ in all haloes of all sizes is calculated with $m_h \rightarrow 0$ (Eq. (15)), i.e. $M_h(a) = \Lambda_m(m_h = 0, a)$ that increases with time.

cade process, combined with acceleration fluctuations, improves our understanding of the empirical acceleration a_0 in BTFR.

Second, a constant rate of the energy cascade ε_u is expected in certain ranges of halo mass scales, that is, the propagation range, where ε_u is independent of the mass scale m_h (Fig. 14). If this is not the case, there would be a net accumulation of energy on some intermediate-mass scale below m_h^* . We exclude this possibility because we require the statistical structures of the haloes to be self-similar and scale-free for haloes smaller than m_h^* . This leads to scale-independent cascade rates up to a critical mass m_h^* . Mass/energy cascaded from small scales is consumed to grow haloes beyond the propagation range, i.e., a deposition range. These fundamental concepts can be rigorously formulated and demonstrated by N-body simulations, along with the value of the rate of cascade ε_u . A similar analysis can also be extended to the mass and energy flow in galaxy bulges for relevant scaling laws and dynamic evolution of galaxies and supermassive black holes [44].

To quantify the mass and energy cascade, we first introduce a cumulative mass function $\Lambda_m(m_h, a)$ that represents the total mass in all haloes greater than a mass scale m_h ,

$$\Lambda_m(m_h, a) = \int_{m_h}^{\infty} M_h(a) f_M(m, m_h^*) dm, \quad (15)$$

where a is the scale factor and M_h is the total mass in all haloes of all sizes. Here, $f_M(m_h, m_h^*)$ is the halo mass function that gives the probability distribution of the total mass M_h in haloes of different mass m_h . Figure 9 plots the variation of the cumulative mass function $\Lambda_m(m_h, a)$ with halo mass m_h and redshifts z . The total halo mass M_h can be obtained by setting $m_h \rightarrow 0$ in Eq. (15), i.e. $M_h(a) = \Lambda_m(m_h \rightarrow 0, a)$ that increases with time.

The mass flux (Π_m) across haloes of different sizes reads

$$\begin{aligned} \Pi_m(m_h, a) &= - \int_{m_h}^{\infty} \frac{\partial}{\partial t} [M_h(a) f_M(m, m_h^*)] dm, \\ &= - \frac{\partial}{\partial t} \left[\int_{m_h}^{\infty} M_h(a) f_M(m, m_h^*) dm \right] = - \frac{\partial \Lambda_m}{\partial t}. \end{aligned} \quad (16)$$

The change of total mass Λ_m above scale m_h equals the mass cascaded from scales below scale m_h . As shown in the schematic plot

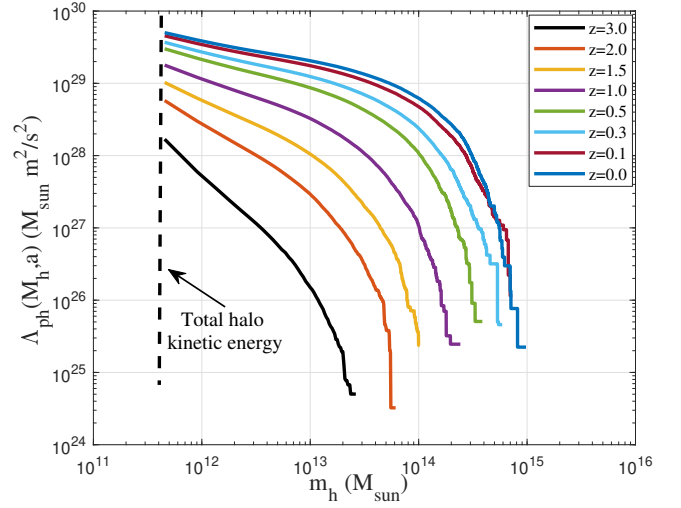


Figure 10. The variation of cumulative halo kinetic energy $\Lambda_{ph}(m_h, a)$ with halo mass scale m_h at different redshifts z , i.e., the kinetic energy from the mean velocity v_h (the motion of entire halo) due to inter-halo interactions on large scales in the linear regime.

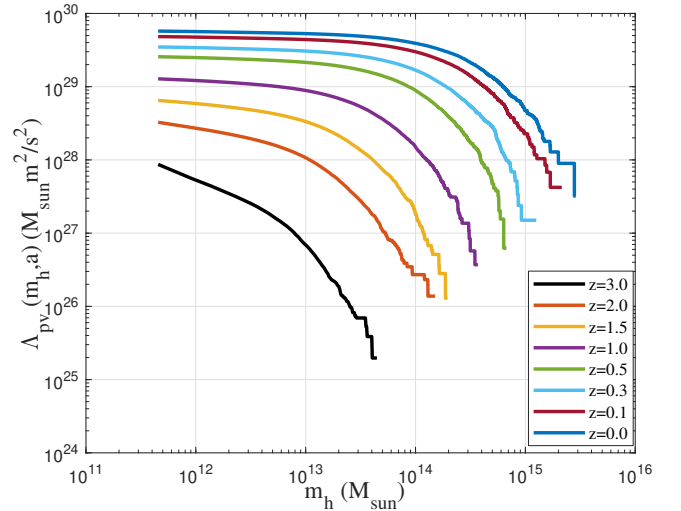


Figure 11. The variation of cumulative halo kinetic energy $\Lambda_{pv}(m_h, a)$ with halo mass scale m_h at different redshifts z , i.e. the kinetic energy from the velocity fluctuation v_{hp}^i (Eq. (4)) due to intra-halo interactions on small scales in the nonlinear regime.

in Fig. 8, all masses cascaded from the smallest scale are propagated through the propagation range and are consumed mainly to grow haloes greater than m_h^* . The scale-independent mass flux in the propagation range reads

$$\varepsilon_m(a) \equiv \Pi_m(m_h, a) \quad \text{for } m_h < m_h^*. \quad (17)$$

Next, velocity v_{hp} of every halo particle can be decomposed into mean velocity v_h and velocity fluctuation v_{hp}^i according to Eq. (4). Similarly, the kinetic energy of each halo particle can be decomposed, that is, the halo kinetic energy from the mean velocity $K_{ph} = v_h^2/2$ and the virial kinetic energy $K_{pv} = (v_{hp}^i)^2/2$ from the velocity fluctuation v_{hp}^i .

Similarly to the cumulative mass function Λ_m in Eq. (15), the cumulative kinetic energies (Λ_{ph} and Λ_{pv}) can be introduced to

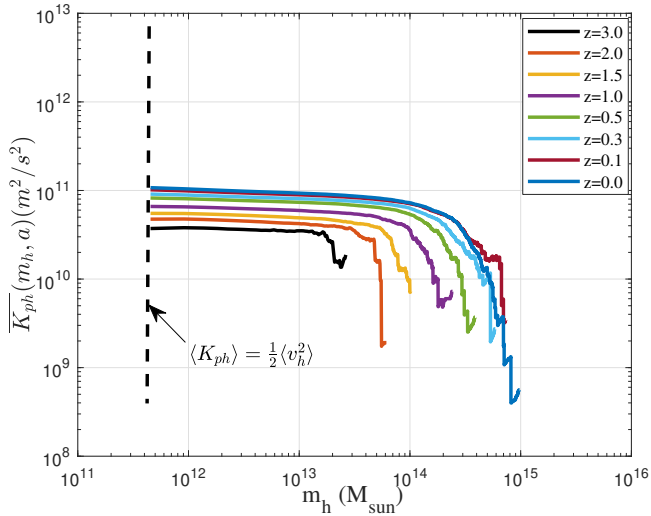


Figure 12. The variation of mean halo kinetic energy $\overline{K_{ph}}$ with halo mass scale m_h at different redshifts z . The mean halo kinetic energy $\langle K_{ph} \rangle$ in all haloes of all sizes is denoted as the dashed line with $m_h \rightarrow 0$, i.e. $\langle K_{ph} \rangle = \overline{K_{ph}}(m_h \rightarrow 0, a)$ that is also related to the velocity dispersion $\langle v_h^2 \rangle$ in Fig. 5. The time evolution of $\langle K_{ph} \rangle \propto t^{2/3}$ is shown in Fig. 15.

represent the total kinetic energies K_{ph} and K_{pv} in all haloes greater than the mass scale m_h ,

$$\Lambda_{ph}(m_h, a) = \int_{m_h}^{\infty} M_h(a) f_M(m, m_h^*) K_{ph} dm, \quad (18)$$

$$\Lambda_{pv}(m_h, a) = \int_{m_h}^{\infty} M_h(a) f_M(m, m_h^*) K_{pv} dm,$$

Using Virgo simulations (SCDM), Figs. 10 and 11 present the variation of the cumulative halo kinetic energy Λ_{ph} and the virial kinetic energy Λ_{pv} with halo mass scale m_h at different redshifts z .

Next, using the cumulative kinetic energy and the cumulative mass Λ_m , we can calculate the mean (specific) halo kinetic energy $\overline{K_{ph}}$ and the mean (specific) virial kinetic energy $\overline{K_{pv}}$ (energy per unit mass) in all haloes above any mass scale m_h , that is,

$$\overline{K_{ph}} = \frac{\Lambda_{ph}}{\Lambda_m} \quad \text{and} \quad \overline{K_{pv}} = \frac{\Lambda_{pv}}{\Lambda_m}. \quad (19)$$

Figures 12 and 13 plot the variation of the halo kinetic energy $\overline{K_{ph}}$ and the virial kinetic energy $\overline{K_{pv}}$ with the mass scale m_h . The halo kinetic energy is relatively independent of m_h . The virial kinetic energy increases with the mass of the halo m_h as $\overline{K_{pv}} \propto m_h^{2/5}$ for larger haloes with mass $m_h \rightarrow \infty$ [43]. Both kinetic energies increase with time but with different scalings because of the distinct nature of intra- and inter-halo interactions in the linear and nonlinear regimes.

The energy cascade is often associated with the kinetic energy contained in the random velocity fluctuations or $\overline{K_{pv}}$. Next, we will focus on the cascade of the specific virial kinetic energy K_{pv} , which is due to the nonlinear interactions and fluctuations on small scales. The rate of cascade for (specific) virial kinetic energy K_{pv} is defined as (similarly to the mass flux defined in Eq. (16))

$$\Pi_{pv}(m_h, a) = -\frac{\partial}{\partial t} (\overline{K_{pv}}) = -\frac{\partial}{\partial t} \left(\frac{\Lambda_{pv}}{\Lambda_m} \right) \quad (20)$$

$$= -\frac{\partial}{\partial t} \int_{m_h}^{\infty} \frac{M_h(a) f_M(m, m_h^*) K_{pv}}{\int_{m_h}^{\infty} M_h(a) f_M(m, m_h^*) dm} dm,$$

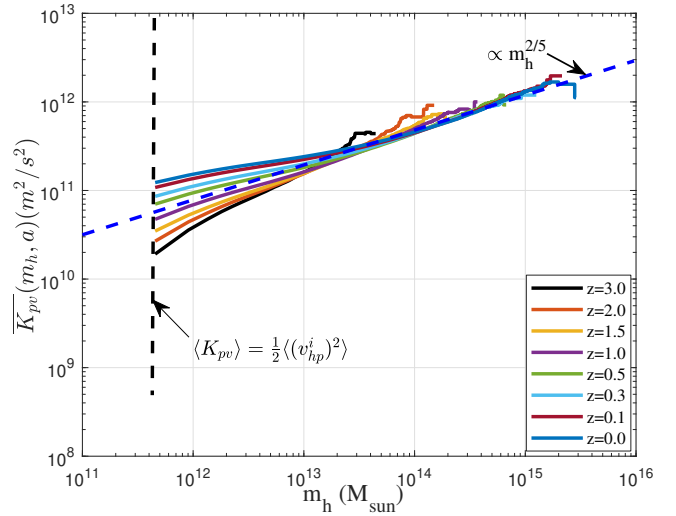


Figure 13. The variation of mean virial kinetic energy $\overline{K_{pv}}$ with halo mass scale m_h at different redshifts z . The mean virial kinetic energy $\langle K_{pv} \rangle$ in all haloes of all sizes is denoted as the dashed line with $m_h \rightarrow 0$. Here, $\langle K_{pv} \rangle = \overline{K_{pv}}(m_h \rightarrow 0, a)$ is also related to the velocity dispersion $\langle (v_{hp}^i)^2 \rangle$ in Fig. 5. This figure will be used to compute the rate of the energy cascade ϵ_u in Fig. 14. The time evolution of virial kinetic energy K_{pv} (the non-linear regime with $\langle K_{pv} \rangle \propto t^1$ is also shown in Fig. 15). The virial kinetic energy follows a 2/5 scaling for large haloes, where $\overline{K_{pv}} \propto m_h^{2/5}$.

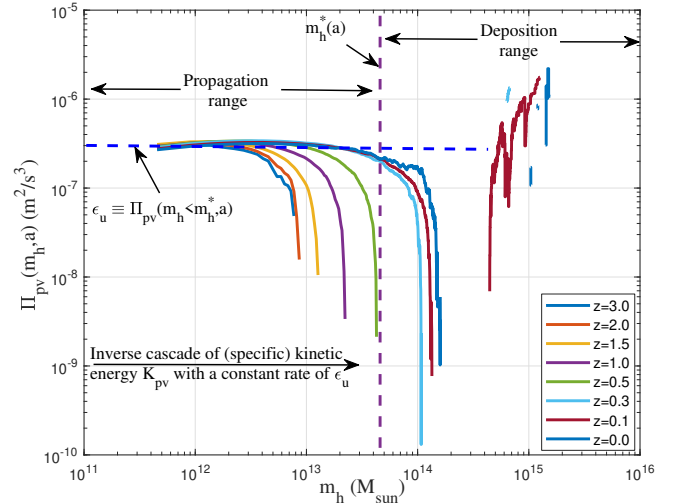


Figure 14. The variation of the rate of energy cascade $\Pi_{pv}(m_h, a)$ (using Eq. (20) and data in Fig. 13) with halo mass scale m_h at different redshifts z . A scale-independent constant rate of ϵ_u can be clearly identified in the propagation range for an inverse cascade of virial kinetic energy K_{pv} from small scales to larger scales. That rate is also relatively independent of time and is around $-3 \times 10^{-7} m^2/s^3$ (also see Fig. 15). This is an important quantity that connects the velocity and acceleration fluctuations in Section 5. The (purple) dashed line denotes the characteristic mass m_h^* at $z = 0$.

where $\overline{K_{pv}}$ is defined in Eq. (19), i.e., the specific virial kinetic energy in all haloes greater than m_h . The inverse cascade (transfer) of the virial kinetic energy K_{pv} from all scales below m_h leads to the change of K_{pv} on all scales above m_h , that is, the change of $\overline{K_{pv}}$ with time. Therefore, Eq. (20) describes the transfer of specific virial kinetic energy (K_{pv}) from all haloes below the scale m_h to all haloes above the scale m_h at a rate of Π_{pv} , i.e. the rate of energy cascade.

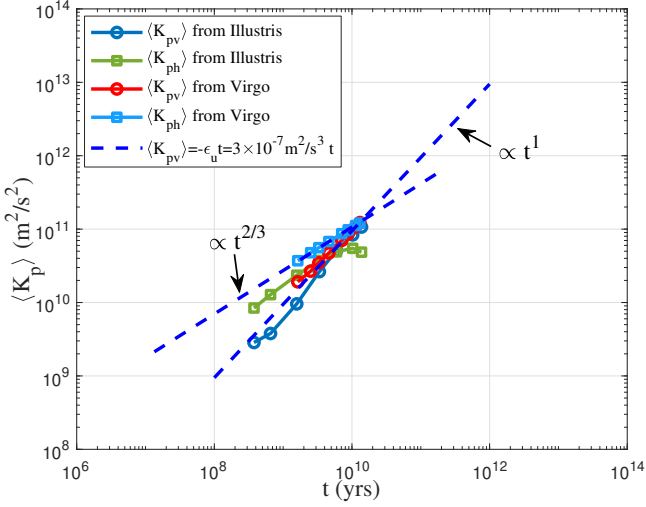


Figure 15. The variation of the mean specific halo kinetic energy (energy per unit mass) $\langle K_{ph} \rangle$ and virial kinetic energy $\langle K_{pv} \rangle$ (unit: m^2/s^2) for all halo particles from Virgo and Illustris-1-Dark simulations. Simulations confirm a constant rate of the energy cascade $\epsilon_u = -3 \times 10^{-7} m^2/s^3$. Due to the long-range inter-halo interactions with particles from different haloes, $\langle K_{ph} \rangle$ increases with time in the early matter dominant universe (i.e., the linear regime with $\langle K_{ph} \rangle \propto t^{2/3}$). In the Illustris simulation, it slightly decreases at low redshift in the dark energy dominant universe due to the accelerated expansion. Due to intra-halo interactions with particles from the same halo, the virial kinetic energy K_{pv} increases as $\langle K_{pv} \rangle \propto -\epsilon_u t$ on small scales (the non-linear regime). Dark energy has smaller effects on $\langle K_{pv} \rangle$ because of bounded structures on small scales.

Figure 14 plots the variation of Π_{pv} with the mass scale m_h and the redshifts z . The mean (specific) virial kinetic energy $\overline{K_{pv}}$ in Fig. 13 was used to calculate the cascade rate Π_{pv} in this figure. The simulation confirms that the rate of the energy cascade Π_{pv} is independent of the mass scale m_h and the time t in the propagation range $m_h < m_h^*$ in Fig. 8 since the statistical structures of the haloes should be self-similar and scale-free for haloes smaller than m_h^* . Therefore, in the propagation range, we can write

$$\epsilon_u \equiv \Pi_{pv}(m_h, a) \quad \text{for } m_h < m_h^*, \quad (21)$$

where ϵ_u is a very important constant that reflects the rate of energy cascade across haloes of different sizes. The physical meaning and impact of the scale-independent rate of cascade were further discussed for the structure and evolution of dark matter haloes [50] and galaxies [44].

Acceleration and velocity fluctuations are connected by ϵ_u in Eq. (24). With continuous injection of virial kinetic energy K_{pv} at a constant rate of ϵ_u on the smallest scale (mass m_X in Fig. 8), we expect the total K_{pv} in all haloes of all sizes to be proportional to time t , that is, $\langle K_{pv} \rangle \propto -\epsilon_u t$, as shown in Fig. 15. Figure 15 presents the evolution of the mean specific halo kinetic energy $\langle K_{ph} \rangle$ and the virial kinetic energy $\langle K_{pv} \rangle$ for all halo particles, i.e. the specific kinetic energy $\overline{K_{ph}}$ and $\overline{K_{pv}}$ in Figs. 12 and 13 with the limit $m_h \rightarrow 0$ (dashed lines). The data in Figs. 12 and 13 were used to plot the time evolution. A constant rate of the energy cascade $\epsilon_u = -3 \times 10^{-7} m^2/s^3$ can be confirmed as the proportional constant for $\langle K_{pv} \rangle$ (that is, $\langle K_{pv} \rangle \propto -\epsilon_u t$), where $\epsilon_u < 0$ represents the inverse cascade from small to large scales). The halo kinetic energy $\langle K_{ph} \rangle \propto a \propto t^{2/3}$ is due to inter-halo interactions on large scales, which is in the linear regime. In the Illustris simulation, it levels off at low redshift z because of the effect of dark energy. While on

small scales or in the non-linear regime, the virial kinetic energy $\langle K_{pv} \rangle \propto -\epsilon_u t$ is due to the inverse cascade of the kinetic energy. The virial kinetic energy is less affected by dark energy because of the bounded halo structure on small scales.

In summary, this section introduces the concept of energy cascade in dark matter. The kinetic energy is inversely cascaded from small to large scales at a constant rate ϵ_u . N-body simulations confirm a constant value of $\epsilon_u \approx -3 \times 10^{-7} m^2/s^3$ (Figs. 14 and 15). The same value of this fundamental constant can also be obtained from Illustris simulations and discussed elsewhere [43, 48, 49, 50]. In the next section, we will use these results to connect the acceleration and velocity fluctuations and identify the critical acceleration a_c (the scale of fluctuation).

5 THE CRITICAL ACCELERATION A_C FROM ENERGY CASCADE

The energy cascade in dark matter is closely related to velocity and acceleration fluctuations, where the constant rate of the energy cascade ϵ_u obtained in Fig. 14 can be directly calculated from these fluctuations (Eq. (24)). To demonstrate this, consider an elementary merging between a halo and a single merger, which facilitates the continuous energy cascade across haloes of different scales. In a finite time interval Δt , the merging of hierarchical structures might involve multiple substructures merging into a single large structure. For an infinitesimal time interval dt , that process should involve the merging of two and only two substructures (Fig. 16) such that the two-body merging is the most elementary and frequent process for structures formation [51]. The continuous two-body merging between the halo and single mergers facilitates the hierarchical structure formation and mass and energy cascade in Fig. 8.

Now consider a typical two-body merging for a dark matter halo of mass m_h (Fig. 16). This halo involves velocity and acceleration fluctuations with a critical velocity $u_c \equiv |\mathbf{u}|$ and a critical acceleration $a_c \equiv |\mathbf{a}|$, representing the scale of velocity and acceleration fluctuations, respectively. These are also the RMS velocity fluctuation (v_{hp}^i) and the acceleration fluctuation (a_{hp}^i) for all halo particles in Eq. (4) and Figs. 4 and 5. Figure 16 plots the instantaneous moment of a typical two-body merging when a single merger with a mass m , a velocity vector \mathbf{u} due to the velocity fluctuations, and an acceleration vector \mathbf{a} due to the acceleration fluctuations, merging with a halo of mass m_h . The single merger is right on the halo boundary (dashed line) at the moment of merging.

i) We focus on the instantaneous moment of merging such that the single merger is right on the halo boundary. After this moment, the halo of mass m_h will move to the next mass scale $m_h + m$, that is, the cascade of mass m_h from the scale m_h to larger mass scales $m_h + m$ (Fig. 8). Now, we focus on the energy cascade that is associated with the mass cascade. Figure 14 describes the calculation of the rate of the energy cascade ϵ_u based on the definition in Eq. (20). This section provides an alternative way to calculate ϵ_u based on the velocity and acceleration fluctuations;

ii) We focus on the cascade of the (specific) virial kinetic energy due to intra-halo interactions on the nonlinear small scales (Fig. 14). Only velocity and acceleration fluctuations are relevant (Eq. (4)), not the mean halo velocity and the mean halo acceleration. Therefore, both velocity \mathbf{u} and acceleration \mathbf{a} are the fluctuations in velocity and acceleration relative to the center of the halo.

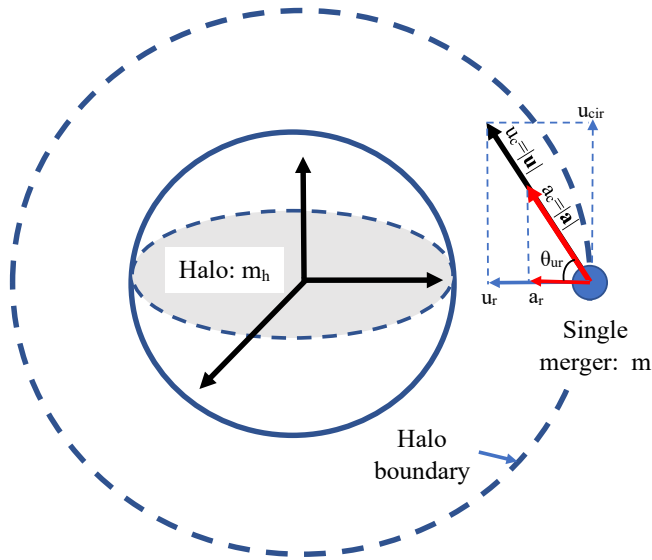


Figure 16. The schematic plot of a typical two-body merging at the instantaneous moment of merging between a halo (mass: m_h) and a single merger (mass: m). The single merger has a typical velocity \mathbf{u} (black) and acceleration \mathbf{a} (red). The dashed line is the boundary of that halo. The angle of incidence satisfies $\cot(\theta_{ur}) = 1/(3\pi)$. Due to the two-body merging, halo mass m_h is cascaded to a larger mass scale at that instantaneous moment, i.e., a halo of mass m_h moving into mass scale $m_h + m$ at that moment. In addition, the specific kinetic energy is simultaneously transferred to larger mass scale at a rate of $\varepsilon_u \propto \mathbf{a} \cdot \mathbf{u} \propto a_c u_c$ (Eq. (24)) at that moment.

iii) Due to the Zeldovich approximation [52] in the linear regime, a single merger, as an out-of-halo particle before merging, should have its velocity aligned with the direction of force or acceleration, that is, $\partial \mathbf{u} / \partial t = H \mathbf{u} / 2$ on large scales. Therefore, at the halo boundary, the velocity vector \mathbf{u} and the acceleration vector \mathbf{a} of a single merger are more likely to align with each other, that is, \mathbf{u} and \mathbf{a} point in the same direction at the moment of merging, as shown in Figs. 16 and 17.

iv) Due to the gravity of the halo to merge with, the single merger right on the boundary (dashed line) has a relative motion towards the center of the halo $u_r = u_c \cos(\theta_{ur})$ (radial velocity) and a radial acceleration with $a_r = a_c \cos(\theta_{ur})$. The angle of incident θ_{ur} can be found as follows. The halo mass m_h satisfies

$$m_h = \frac{4}{3} \pi r_h^3 \Delta_c \bar{\rho} \Rightarrow u_{cir} = \sqrt{\frac{G m_h}{r_h}} = H r_h \sqrt{\frac{\Delta_c}{2}} = 3\pi u_r, \quad (22)$$

where r_h is the virial size of the halo, $\Delta_c = 18\pi^2$ is the critical halo density from a spherical collapsed model [53], and u_{cir} is the circular velocity at the boundary of halo. The Hubble parameter $H^2 = 8\pi G \bar{\rho} / 3$, where $\bar{\rho}(t)$ is the mean density of matter. Due to the stable clustering hypothesis for virialized haloes, there is no stream motion between particles in physical coordinates. In this sense, the peculiar motion cancels out the Hubble flow, and the hypothesis equivalently states that the peculiar radial velocity $u_r = H r_h$ in Eq. (22). Therefore, the angle of incidence reads (on average)

$$\cos(\theta_{ur}) \approx \cot(\theta_{ur}) = \frac{u_r}{u_{cir}} = \frac{1}{3\pi}. \quad (23)$$

Figure 16 represents a simple picture at the moment of a two-body merging, from which we hope to gain more insight.

From the above discussion, an alternative approach is presented here to estimate the constant rate of the energy cascade ε_u that

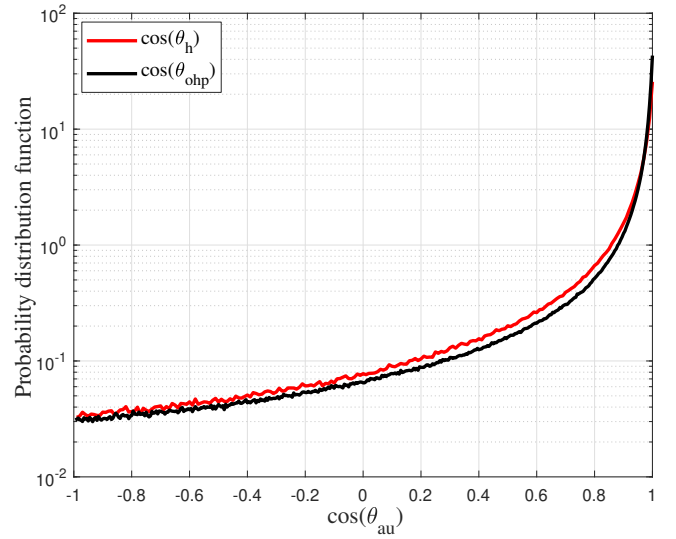


Figure 17. The probability distribution of $\cos(\theta)$ from Virgo N-body simulations for the angle θ between velocity and acceleration vectors. Here, θ_h represents the angle between halo velocity \mathbf{v}_h and halo acceleration \mathbf{a}_h in Eq. (4), θ_{ohp} represents the angle between velocity and acceleration for "out-of-halo" particles. This plot shows the velocity and acceleration of out-of-halo particles and haloes aligned on large scales pointing in the same direction. Most haloes and out-of-halo particles have small angles with $\cos(\theta) \approx 1$.

should give the same value as we obtained from the energy cascade in mass space (14). The inverse cascade of mass and kinetic energy is facilitated by a series of halo merging with single mergers (Fig. 8). Upon each merging event, the mass is cascaded from a smaller scale m_h to a larger scale $m_h + m$. Simultaneously, associated with the mass cascade, the kinetic energy is also transferred from the smaller to the larger mass scales that come from the change in the kinetic energy of that single merger at the instant of merging. Only relative motion along the radial direction is relevant for the energy cascade (Fig. 16), which is due to the intra-halo interaction on small scales. Motion in the tangential direction does not contribute to the energy cascade. Therefore, for a single merger with a critical velocity u_c and a critical acceleration a_c , the rate of the energy cascade ε_u can be simply treated as the change in specific kinetic energy $u_r^2/2$ of that single merger, i.e.,

$$\varepsilon_u \propto -\frac{1}{2} \frac{d(u_r^2)}{dt} = -a_r u_r = -a_c u_c \cos^2(\theta_{ur}), \quad (24)$$

where $\varepsilon_u < 0$ for inverse cascade of kinetic energy from small to large scales, and $\cos(\theta_{ur}) \approx \cot(\theta_{ur})$ for θ_{ur} close to $\pi/2$ in Eq. (23). Here, the critical velocity and acceleration, or the scales of the velocity and acceleration fluctuations, are $u_c \equiv |\mathbf{u}| = \text{std}(v_{hp}^i)$ and $a_c \equiv |\mathbf{a}| = \text{std}(a_{hp}^i)$. Figures 4 and 5 present the redshift evolution of u_c and a_c . This picture also reveals that the energy cascade in the dark matter flow is directly associated with the mass cascade. The mass and energy cascade are tightly coupled together [50]. In contrast, the energy cascade in turbulence is facilitated by the deformation of the vortex structure, that is, by a vortex stretching mechanism [54]. Mass cascade does not exist in incompressible turbulence.

Combining Eqs. (23) and (24) together, the critical acceleration $a_c(a)$ can be related to the rate of the cascade ε_u as

$$a_c(a) \approx -\Delta_c \frac{\varepsilon_u}{u_c} = -18\pi^2 \frac{\varepsilon_u}{u_c} \propto a^{-3/4} \propto t^{-1/2}. \quad (25)$$

With $u_c = 496 \text{ km/s}$ at $z = 0$ from Fig. 5 and the constant rate of the

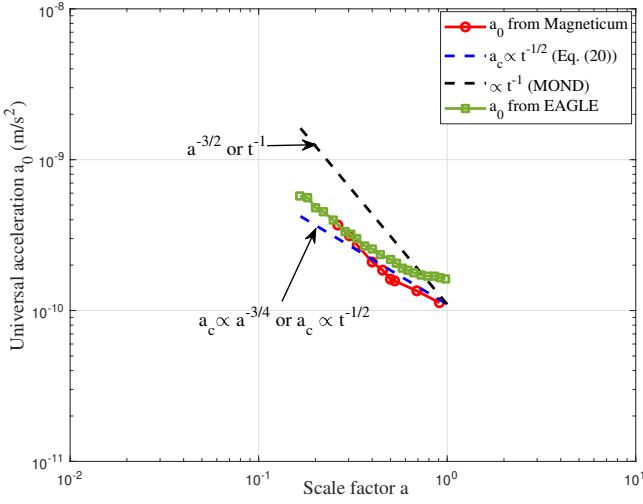


Figure 18. The variation of the universal acceleration a_0 extracted from a large sample of galaxies in cosmological hydrodynamical Magneticum simulations (red circles) [55] and the EAGLE (green squares) [56]. The predicted critical acceleration a_c of dark matter varies with time as $a_c \propto a^{-3/4} \propto t^{-1/2}$ in Eq. (26). The critical acceleration a_c matches the universal MOND acceleration a_0 extracted from Magneticum, which suggests the potential relations between two accelerations (Section 7). The time evolution $a_0 \propto t^{-1}$ suggested by MOND was also plotted for comparison, which seems not to agree with the simulation. Our model predicts $a_0 \propto t^{-1/2}$ that matches better with the N-body hydrodynamic simulations.

energy cascade $\varepsilon_u = -3 \times 10^{-7} m^2/s^3$ from Fig. 14, the critical scale a_c for acceleration fluctuation reads

$$a_c(z) = a_{c0} a^{-3/4} \propto a_{c0} t^{-1/2}, \quad \text{where} \quad (26)$$

$$a_{c0} \equiv a_c(z=0) \approx 1.1 \times 10^{-10} m/s^2,$$

where a_{c0} is the critical acceleration at $z=0$. Here, the velocity fluctuations and the acceleration fluctuations are related to each other through the rate of the energy cascade ε_u . Furthermore, the redshift dependence of the critical acceleration a_c is predicted to be $a_c(a) \propto a^{-3/4} = (1+z)^{3/4}$ with a value of $a_c = 1.1 \times 10^{-10} m/s^2$ at $z=0$, which can be clearly confirmed by the N-body simulations in Fig. 4.

6 SIMULATIONS AND OBSERVATIONS FOR REDSHIFT EVOLUTION OF a_c

Return to the baryonic Tully-Fisher relation (BTFR in Eq. (1)), the empirical acceleration $a_0 \approx 10^{-10} m/s^2$ matches the value of the critical acceleration a_c of dark matter in Eq. (26). Over the years, Modified Newtonian Dynamics (MOND) has been proposed to explain the empirical BTFR, where a_0 is a universal acceleration scale in MOND. In this section, we show that the critical acceleration a_{c0} from the acceleration fluctuation matches the empirical acceleration a_0 in BTFR and MOND. More importantly, the predicted redshift dependence of $a_c \propto a^{-3/4}$ is consistent with the evolution of a_0 from hydrodynamic simulations, as shown in Fig. 18.

For example, in Magneticum simulation [55], the relation between the baryonic acceleration and the total acceleration, i.e., the rotational acceleration relationship (RAR), can be extracted from a large sample of galaxies. Universal acceleration a_0 can be identified from the RAR relation at different redshifts z . Figure 18 presents the redshift variation of the universal acceleration a_0 from the Magneticum simulations (red circle). Our theory predicts the critical acceleration of

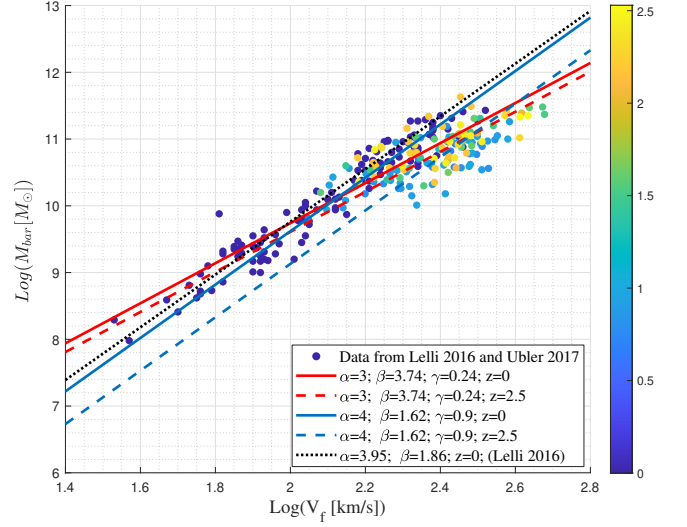


Figure 19. The BTFR for our 253 samples of galaxies color-coded by the redshift of each galaxy. The first 118 galaxies are taken from [62] at $z=0$ (blue dots). The other 135 galaxies are taken from [60] with various redshift $0.6 < z < 2.5$. The critical line plots the best fit of 118 local galaxies from [62]. The red solid and dashed lines plot the best free fit of all 253 galaxies at $z=0$ and 2.5, respectively, when including γ for redshift dependence (Eq. (27)), with best $\gamma = 0.24$. The blue solid and dashed lines plot the best fit of 253 galaxies with a fixed slope $\alpha = 4$, where the best $\gamma = 0.9$. Relevant parameters (α , β_0 , and γ) can be found from black dashed lines in Fig. 20. Both cases confirm a positive γ such that galaxies of fixed mass rotate faster at higher redshift. Larger slope α exhibits stronger redshift dependence.

dark matter $a_c \propto a^{-3/4} \propto t^{-1/2}$ (blue dashed line for Eq. (26)) that matches the acceleration a_0 obtained from the hydrodynamic simulations. Furthermore, the redshift dependence of a_0 is obviously shallower than $\propto t^{-1}$ (black dashed line), which is proposed from the coincidence in MOND theory [57], that is, $a_0 = cH/(2\pi) \propto t^{-1}$, where c is the speed of light. This conclusion can also be confirmed by the acceleration a_0 obtained from the EAGLE simulation results (green squares) [56], which is consistent with the scaling $a_c \propto a^{-3/4} \propto t^{-1/2}$. The larger a_c at higher redshift means galaxies of fixed mass rotate faster at higher redshift with the scaling $v_f \propto (1+z)^{3/16}$ from Eq. (1).

The Millennium Simulation with a large sample of 3×10^7 galaxies of various morphologies also confirms this redshift evolution of the BTFR. In panel (c) of Fig. 14 in [58], when comparing against the rotation at $z=0$, the galaxies of baryonic mass $M_b = 4 \times 10^6 M_\odot$ rotate $\times 1.4$ faster at $z=4.89$ and $\times 1.6$ faster at $z=10.07$, consistent with the scaling of $v_f \propto (1+z)^{3/16}$. This also confirms a larger a_0 at a higher redshift, consistent with our predictions.

Limited observational evidence also exists for galaxies of fixed mass rotating faster at higher redshifts [59, 60, 61]. We provide a brief discussion here by generalizing the original BTFR in Eq. (1) to include the redshift dependence,

$$\log M_b = \alpha \log v_f - \gamma \log(1+z) + \beta_0, \quad (27)$$

where α is a slope parameter for BTFR. Here, β_0 is an intercept parameter at $z=0$ that can be related to the critical acceleration at $z=0$ (Eq. (28)). Redshift parameter γ is introduced for the redshift dependence of the intercept of BTFR. For galaxies of fixed mass M_b , the larger γ means the stronger redshift dependence and the larger rotation velocity v_f at a high redshift.

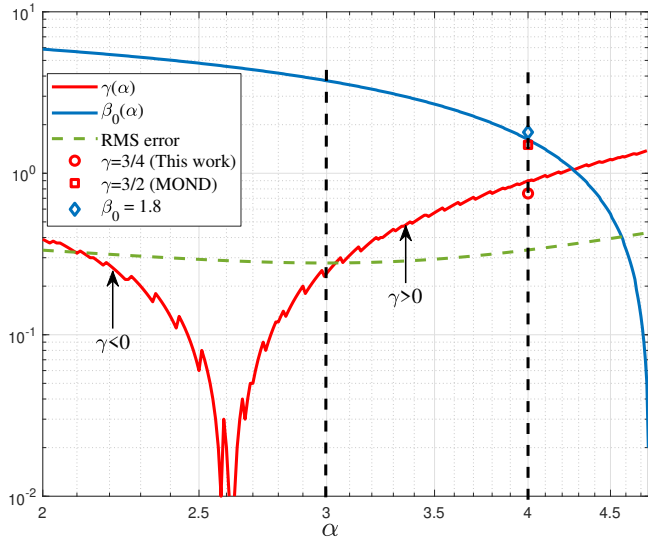


Figure 20. The variation of the redshift parameter γ and intercept parameter β_0 in Eq. (27) fitting to all 253 galaxies for different fixed slope parameter α . The RMS error of fitting is plotted as a dashed line. The BTFR with minimum RMS error for free fit among all different α is found at $\alpha = 3$ and plotted as red lines in Fig. 19. The BTFR for fixed $\alpha = 4$ is plotted as blue lines in Fig. 19. The redshift parameter γ is positive between a range of $3 < \alpha < 4$, confirming a redshift-dependent BTFR. The larger α , the larger γ , and the stronger redshift dependence of BTFR. At $\alpha = 4$, the predicted β_0 is around 1.8 (diamond from Eq. (28)). The predicted values of $\gamma = 3/4$ from this work (red circle) and $3/2$ from MOND (red square) are also shown. From these data, the critical acceleration a_0 is redshift dependent, with a smaller dependence than MOND prediction $a_0 \propto (1+z)^{3/2}$, and in better agreement with simulations (Fig. 18) and our model of $a_0 \propto (1+z)^{3/4}$.

Specifically, for slope parameter $\alpha = 4$ in Eq. (1),

$$\alpha = 4 \quad \beta_0 = -\log\left(\frac{Ga_c M_\odot}{10^{12} m^4 / s^4}\right) = 1.8. \quad (28)$$

We assume a general power-law redshift dependence of the critical acceleration $a_0 \propto (1+z)^\gamma$. Our theory predicts $\gamma = 3/4$ if a_0 represents the acceleration fluctuations in dark matter, while MOND predicts either $\gamma = 3/2$ if $a_0 \propto cH$ (Fig. 18) or $\gamma = 0$ if $a_0 \propto cH_0$ is independent of z . We expect to estimate the value of γ from local and high-redshift observations.

Figure 19 presents the observed baryonic mass M_b and rotation velocity v_f for 118 local galaxies at $z = 0$ taken from [62] and 135 high-redshift galaxies with various redshift $0.6 < z < 2.5$ taken from [60] (symbols colored by redshift). The standard approach to obtain the BTFR is the two-parameter fit of slope α and intercept β_0 [59, 60, 62]. In contrast, we perform the least-squares fit of three parameters α , β_0 , and γ in Eq. (27) for all 253 galaxies to evaluate the redshift dependence. For every fixed slope α , Fig. 20 presents the best fitting of γ and β_0 in Eq. (27). The corresponding RMS error of fitting is also presented. The error slowly increases toward $\alpha = 4$ with the minimum error obtained at $\alpha = 3$ (dashed black line). The corresponding BTFR for $\alpha = 3$ and 4 were also presented in Fig. 19 (red and blue lines). Both figures confirm a redshift-dependent BTFR such that galaxies of fixed mass rotate faster at higher redshifts. Data suggests a positive γ increasing with α . More importantly, for $\alpha = 4$, observation data also suggests γ is smaller than the MOND prediction ($\gamma = 3/2$) and is in better agreement with our prediction $\gamma = 3/4$, which supports the origin of critical acceleration a_0 from

acceleration fluctuations. Future study requires more high quality high-redshift data.

The time evolution of $a_c \propto (1+z)^{3/4} \propto t^{-1/2}$ in Eq. (26) offers a powerful test to distinguish between MOND and Λ CDM with a redshift dependent a_c . The coincidence between the critical acceleration of dark matter a_c and the universal acceleration a_0 in BTFR and MOND suggests a potential connection between two accelerations. In the next Section, we will briefly discuss this connection.

7 THE ORIGIN OF UNIVERSAL ACCELERATION a_0

Similarly to the critical velocity scale u_c due to the fluctuation of the velocity, there exists a critical acceleration a_c due to the fluctuation of the acceleration (Figs. 3 and 4). Note that the critical acceleration a_c at $z=0$ matches the empirical acceleration a_0 in BTFR and also the universal MOND acceleration. This suggests that a_0 could be an intrinsic property of Λ CDM cosmology due to the acceleration fluctuations in dark matter. The value and origin of a_0 in BTFR is still empirical and phenomenological without a good theory. In this section, we briefly discuss the connection between empirical acceleration a_0 and critical acceleration a_c in dark matter.

First, the modified Newtonian Dynamics (MOND) is a popular empirical model that reproduces the same astronomical observations without invoking the dark matter hypothesis [25]. The basic idea of MOND is to introduce a universal acceleration a_0 . Standard Newtonian mechanics $F = ma$ is recovered when baryon acceleration $a \gg a_0$. For the "deep-MOND" regime with $a \ll a_0$, Newtonian mechanics should be modified to $F = ma^2/a_0$, that is, the external force $F \propto a^2$. In the "deep-MOND" regime, for a galaxy with a total baryonic mass M_b , the dynamics for a given baryon particle far from the center of the galaxy is given by (with acceleration $a = v_f^2/r$, where r is the distance):

$$\frac{F}{m} = \frac{GM_b}{r^2} = \frac{(v_f^2/r)^2}{a_0} \Rightarrow v_f^4 = GM_b a_0, \quad (29)$$

which is the BTFR with a rotation velocity v_f in Eq. (1).

The universal MOND acceleration a_0 (or the empirical BTFR acceleration) might originate from the critical acceleration a_c due to fluctuations in dark matter acceleration. Let us consider baryons dispersing and mixing with a fluctuating dark matter fluid. The self-gravitating collisionless dark matter fluid has an intrinsic critical velocity scale u_c and a critical acceleration scale a_c due to respective velocity and acceleration fluctuations (Sections 2 and 3). The rate of the energy cascade can be related to the velocity and acceleration fluctuations as $\varepsilon_u \propto -a_c u_c$ (Eq. (24)) (Section 5). For the entire halo, the total mass of dark matter is dominant over the mass of baryons. However, in the core region of haloes (bulge), the baryonic mass (star plus gas) can be dominant over the mass of dark matter.

Consider baryonic particles on the outskirts of the halo with mass m_b , velocity u_b , and acceleration $a_b = du_b/dt$, moving under an external driving force F_b . The baryons interact with dark matter through gravity only so that the baryons in the halo outskirts are in equilibrium with dark matter and share the same rate of energy cascade such that $\varepsilon_u \propto -a_b u_b$ (Eq. (30)). The acceleration of baryons on the outskirts can be extremely small and less than the critical acceleration a_c of the fluctuation, that is, $a_b < a_c$. In this scenario, the effect of fluctuations is dominant over the effect of external force F_b . The acceleration of the baryon particle a_b and the velocity u_b should give the same rate of the energy cascade:

$$-\varepsilon_u \propto a_c u_c = a_b u_b. \quad (30)$$

Next, the external force F_b can be calculated from the time derivative of the specific kinetic energy ε_K . This means the change in the particle kinetic energy equals the power from the external force. Therefore, we write

$$F_b u_b = m_b \frac{d\varepsilon_K(u_b)}{dt} = m_b \frac{d\varepsilon_K(u_b)}{du_b} \frac{du_b}{dt} = m_b u_c a_b, \quad (31)$$

where $\varepsilon_K \propto u_c u_b$ from Eq. (14), i.e., the kinetic energy of baryon particles shares the same form as dark matter particles. Here, the left-hand side is the input of power (the work done by F_b per unit of time) from the external force F_b . The right-hand side shows the change in the kinetic energy of baryons. The work done by F_b increases the kinetic energy ε_K of the baryon. In self-gravitating collisionless dark matter flow, the effective kinetic energy ε_K can be obtained from the maximum entropy distributions [32]. In Eq. (14), the effective kinetic energy follows $\varepsilon_K(v) \propto v^2$ for particles in the core region with low speed or high acceleration ($v \ll v_0$), that is, the standard Newtonian behavior. However, $\varepsilon_K(v) \propto v_0 v$ for high-speed or low-acceleration particles ($v \gg v_0$) in the outskirts of haloes is a unique "non-Newtonian" feature due to the long-range nature of gravity. Here, the velocity scale v_0 plays the role of the critical velocity u_c .

Finally, for baryon particles with $a_b \ll a_c$ or $u_b \gg u_c$ (in the outskirts region of the halo), the specific kinetic energy $\varepsilon_K \propto u_c u_b$ due to the long-range gravity and inter-halo interactions. Substituting this into Eq. (31), the external force can be calculated from Eqs. (30) and (31) as

$$F_b = m_b a_b \frac{u_c}{u_b} = m_b \frac{a_b^2}{a_c}. \quad (32)$$

This result is in agreement with the force in the "deep-MOND" regime. Compared Eq. (32) against Eq. (29), we found that the critical acceleration a_c due to acceleration fluctuations in dark matter plays the role of universal acceleration a_0 in BTFR or MOND. Furthermore, the time evolution of $a_c \propto t^{-1/2}$ in Eq. (26) suggests the same time evolution of $a_0 \propto t^{-1/2}$. This theory offers a powerful test to distinguish between MOND and Λ CDM from observations of the redshift variation of a_0 .

On the other hand, for particles with high acceleration in the halo core region, that is, $a_b \gg a_c$, the effect of external force F_b is dominant over fluctuations. The intra-halo interactions are dominant over inter-halo interactions. The standard Newton law $F_b = m_b a_b$ can be recovered by inserting $\varepsilon_K \propto u_b^2$ from Eq. (14) into Eq. (31).

In short, two key ingredients are necessary for this simple interpretation: i) the constant rate of the energy cascade for both dark matter and baryons (Eq. (30)), and ii) the effective kinetic energy proportional to the speed at a small acceleration (Eq. (14)). With these two ingredients, we may recover the MOND. In conventional wisdom, MOND is a competing empirical theory that falsifies dark matter. In this work, we propose that MOND is an intrinsic feature of and consistent with Λ CDM. Instead of falsifying dark matter, MOND is an effective theory for the dynamics of baryons in equilibrium with self-gravitating collisionless dark matter.

8 RELEVANT PHYSICAL QUANTITIES ON SMALL AND LARGE SCALES

Figure 8 discusses the propagation range between the smallest mass scale m_X and the characteristic halo mass m_h^* . The smallest mass scale depends on the particle mass and free streaming. The smallest structure that can be formed by dark matter particles of any mass has a mass around $m_X = 10^{12} \text{GeV}$ [43]. The propagation range involves

a constant rate of cascade ε_u , which is independent of the mass scale. The value of ε_u is determined in Section 4 (Fig. 14). The velocity and acceleration fluctuations introduce two additional quantities, i.e. the velocity scale u_c and acceleration scale a_c , in the propagation range. In this section, similarly to the application of dimensional analysis in fluid dynamics and turbulence, we will apply dimensional analysis to the flow of collisionless dark matter to determine relevant physical quantities at the small end m_X and the large end m_h^* of the propagation range.

First, let us focus on the large end in Fig. 8. This is the largest halo scale at $z = 0$ (denoted by the subscript A). On that scale, the expansion of the universe is important. The Hubble constant H_0 and the fluctuation scales (u_c and a_c) should play a role on this scale. The corresponding one-dimensional velocity scale is $u_0 = u_c/\sqrt{3}$. The dominant physical constants on this scale are G , ε_u , the critical velocity scale $u_0 \approx 286 \text{km/s}$ from Fig. 5 (or the acceleration fluctuation scale a_c), and the scale factor a (or the Hubble parameter H). Any physical quantity Q on this scale can be expressed as $Q \propto G^x \varepsilon_u^y u_0^z a^p$, where the exponents (x, y, z) can be determined from the dimensional analysis.

Table 1 lists the relevant physical quantities on the largest scale A (at $z = 0$) calculated with values for ε_u , G and u_0 :

$$\begin{aligned} \varepsilon_u &= -3 \times 10^{-7} \text{m}^2/\text{s}^3, \\ G &= 6.67 \times 10^{-11} \text{m}^3/(\text{kg} \cdot \text{s}^2), \\ u_0 &= 286 \text{km/s}. \end{aligned} \quad (33)$$

The length scale $l_A \propto u_0^3/\varepsilon_u = 2.5 \text{Mpc}$ is about the size of the largest halo with a characteristic halo mass $m_A \approx m_h^* \approx 10^{13} M_\odot$. The time scale t_A should be the time (approximately the age of the universe t_0) required to form the largest halo. The density scale $\rho_A \propto \varepsilon_u^2/Gu_0^4$ is the average mass density of the entire halo. If we write the mean dark matter density as (Ω_m is the mass fraction of dark matter),

$$\bar{\rho} = \frac{3H_0^2}{8\pi G} \Omega_m \approx 2 \times 10^{-27} \text{kg}/\text{m}^3, \quad (34)$$

the density contrast $\Delta_c = \rho_A/\bar{\rho}$ can be obtained as

$$\Delta_c = \frac{\rho_A}{\bar{\rho}} = \frac{8\pi}{3\Omega_m} \left(\frac{\varepsilon_u}{H_0 u_0^2} \right)^2 \approx 100. \quad (35)$$

This density contrast is of the same order as the value $\Delta_c = 18\pi^2$ obtained independently from the spherical collapse model [63]. The acceleration scale a_A has already been discussed in detail (Eq. (25)), which is the critical acceleration in fluctuation.

The energy density scale ρ_{eA} is comparable to the energy density of CMB photons (cosmic microwave background). The CMB photons interact with baryons via Thomson scattering, whereas dark matter interacts with baryons via gravity. With all three "phases" (baryons, radiation, and dark matter) in equilibrium on the largest halo scale, the energy density or pressure of the haloes on that scale ρ_{eA} should be comparable to that of the CMB density $\rho_{CMB} \approx 4 \times 10^{-14} \text{J}/\text{m}^3$, that is, the halo pressure on that scale is in balance with the background radiation. Finally, the "effective" kinematic viscosity ν_A is relevant to the adhesion model in large-scale structure formation [35, 64].

The small mass end of the propagation range (or mass scale m_X) was discussed in a separate paper [43]. For cold dark matter that is fully collisionless, the scale-independent cascade rate ε_u (Fig. 14) can be extended down to the smallest mass scale m_X , where quantum effects become important if there are no other known interactions involved except gravity. This is the field of non-relativistic quantum

Quantity	The smallest scale X	The largest scale A of halo at $z = 0$
Length	$l_X = (-G\hbar/\varepsilon_u)^{1/3}$ $=10^{-13}\text{m}$	$l_A = -u_0^3/\varepsilon_u$ $=2.5\text{Mpc}$
Time	$t_X = (-G^2\hbar^2/\varepsilon_u^5)^{1/9}$ $=10^{-7}\text{s}$	$t_A = (-u_0^2\varepsilon_u)$ $=8.6 \times 10^9\text{year}$
Mass	$m_X = (-\varepsilon_u\hbar^5/G^4)^{1/9}$ $=10^{12}\text{GeV}$	$m_A = -u_0^5/(G\varepsilon_u)$ $=4.8 \times 10^{13}M_\odot$
Velocity	$v_X = (\varepsilon_u^2\hbar G/4)^{1/9}$ $=10^{-7}\text{m/s}$	$v_A = u_0$ $=286\text{km/s}$
Acceleration	$a_X = (-\varepsilon_u^7/(\hbar G))^{1/9}$ $=1.11\text{m/s}^2$	$a_A = a_c = -\Delta c \varepsilon_u/u_c$ $=1.1 \times 10^{-10}\text{m/s}^2$ (see Eq. (25))
Energy	$E_X = (-\hbar^7\varepsilon_u^5/G^2)^{1/9}$ $=10^{-9}\text{eV}$	$E_A = -u_0^7/(G\varepsilon_u)$ $=7.8 \times 10^{54}\text{J}$
Density	$\rho_X = (\varepsilon_u^{10}/(\hbar^4 G^{13}))^{1/9}$ $=10^{22}\text{kg/m}^3$	$\rho_A = \varepsilon_u^2/(Gu_0^4)$ $=2 \times 10^{-25}\text{kg/m}^3$
Energy density (pressure)	$\rho_{eX} = (\varepsilon_u^{14}\hbar^{-2}G^{-11})^{1/9}$ $=10^{10}\text{J/m}^3$	$\rho_{eA} = \varepsilon_u^2/(Gu_0^2)$ $=1.6 \times 10^{-14}\text{J/m}^3$
Diffusivity (kinematic viscosity)	$\nu_X = (-\hbar^4 G^4 \varepsilon_u^{-1})^{1/9}$ $=10^{-19}\text{m}^2/\text{s}$	$\nu_A = -u_0^4/\varepsilon_u$ $=2.2 \times 10^{28}\text{m}^2/\text{s}$

Table 1. Relevant physical quantities on large and small ends of the propagation range in Fig. 8.

gravity or Newtonian quantum gravity. Assuming that gravity is the only interaction between dark matter particles (traditionally denoted by X), the dominant constants on the smallest scale (the X scale) are the (reduced) Planck constant \hbar , the gravitational constant G , and the rate of the energy cascade ε_u . Similarly to the large end, any physical quantity Q on this scale can be expressed as $Q \propto G^x \varepsilon_u^y \hbar^z$, where exponents can be determined from the dimensional analysis. With values listed in Eq. (33) and $\hbar = 1.05 \times 10^{-34}\text{kg} \cdot \text{m}^2/\text{s}$, all relevant quantities on the mass scale m_X can easily be found and listed in Table 1. Details can be found in relevant references [43, 48].

9 DARK ENERGY FROM ACCELERATION FLUCTUATIONS

With the critical acceleration scale $a_{c0} \approx 10^{-10}\text{m/s}^2$, an energy density can be naturally related to the acceleration fluctuation as $a_{c0}^2/G \approx 10^{-10}\text{J/m}^3$, which is on the same order as the density of dark energy ρ_{DE0} at $z = 0$. In this section, we briefly discuss a possible model for dark energy as an energy density originating from the acceleration fluctuations of dark matter and compare this model with existing models. Discussions are only briefly presented here in the hope of leading to other suggestions and ideas from the community. Future studies require rigorous thermodynamic treatment for systems involving long-range interactions.

Dark energy, a pervasive form of energy, was proposed to account for the accelerated expansion of the universe. The nature of dark energy has remained elusive for more than a quarter century. A key question of dark energy is whether it is a cosmological constant Λ , or it dynamically evolves, or it arises from the modifications of General Relativity.

For dynamical models of dark energy, the first example is a flat w CDM model, where the evolution of the dark energy density ρ_{DE} involves an equation of state parameter w such that $\rho_{DE} \propto a^{-3(1+w)}$.

Parameter $w=-1$ recovers the standard Λ CDM model with a constant dark energy density. The second example involves a two-parameter parametrization of the equation of state parameter $w(a) = w_0 + w_a(1-a)$ ($w_0 w_a$ CDM model). This model leads to an evolving dark energy density of [65],

$$\rho_{DE} = \rho_{DE0} a^{-3(1+w_0+w_a)} e^{3w_a(a-1)}, \quad (36)$$

The recent results on baryon acoustic oscillations from DESI (Dark Energy Spectroscopic Instrument) provide constraints on two parameters w_0 and w_a when combined with cosmic microwave background and supernova data [66]. These results prefer $w_0 > -1$ and $w_a < 0$ and indicate potential deviations from the standard Λ CDM model with a quickly weakening dark energy at low redshift due to the exponential term in Eq. (36).

We begin with an analogy of the pressure in the kinetic theory of gases. The Maxwell-Boltzmann distribution of gas molecule velocity can be obtained from the maximum entropy principle (Eq. (5)). There exist velocity fluctuations with a typical velocity scale v_{gas} . Kinetic pressure (or energy density) P_{gas} , a macroscopic state variable, is related to the velocity fluctuations (or temperature $k_B T \propto v_{gas}^2$),

$$P_{gas} \propto \rho_{gas} v_{gas}^2, \quad (37)$$

where ρ_{gas} is the density of gas. This suggests a fluctuation (an entropic or random motion) nature of the kinetic pressure P_{gas} . Thermal fluctuations tend to bring a system to its macroscopic state of maximum entropy with a finite pressure P_{gas} . The larger the velocity fluctuations v_{gas}^2 , the higher the temperature T , the greater the entropy contained in the velocity distribution, and the higher kinetic pressure P_{gas} .

For the self-gravitating flow of collisionless dark matter, acceleration fluctuations also exist with a typical scale $a_{c0} \equiv a_c(z=0)$, in addition to the velocity fluctuations (Sections 2 and 5). Similarly to the kinetic pressure in Eq. (37), we postulate the existence of an additional energy density that is due to the acceleration fluctuations of all dark matter. Therefore, in an analog to Eq. (37) for gas pressure, an acceleration-fluctuation-induced energy density ρ_a at $z = 0$ reads (using Eq. (25))

$$\rho_a = A_0 \frac{a_{c0}^2}{G} \approx 2A_0 \times 10^{-10}\text{J/m}^3, \quad (38)$$

which coincidentally is on the same order of dark energy density $\rho_{DE0} = 5 \times 10^{-10}\text{J/m}^3$ at $z = 0$. Here, the dimensionless numerical constant A_0 in Eq. (38) is of unity. Unlike the kinetic pressure in Eq. (37), there is no density involved in Eq. (38) such that this energy density due to acceleration fluctuation is independent of the local matter density. On large scales, it should be relatively homogeneous in space.

Since the acceleration-fluctuation-induced energy density ρ_a , if exists, happens to be on the same order as the dark energy density at $z = 0$ (Eq. (38)), we postulate the dark energy with a possible origin from the acceleration fluctuation $\langle a_p^2 \rangle$ (Fig. 4) such that the dark energy density reads

$$\rho_{DE} = A_0 \frac{\langle a_p^2 \rangle}{G} a^{-\nu_0}, \quad (39)$$

where $\langle a_p^2 \rangle$ is the acceleration fluctuations of all dark matter particles. Here, ν_0 is an exponent of scale factor a that can be constrained from observations. The evolution of the standard deviation of particle acceleration $\text{std}(a_p) = \sqrt{\langle a_p^2 \rangle}$ is presented in Fig. 4 (magenta color).

Since all dark matter particles can be divided into the halo particles with a total mass of M_h and out-of-halo particles, the fluctuations of

all particles can be written as a weighted average involving a mass fraction M_h/M (Here, M is the total mass of all dark matter):

$$\langle a_p^2 \rangle = \langle a_{hp}^2 \rangle \frac{M_h}{M} + \langle a_{op}^2 \rangle \left(1 - \frac{M_h}{M}\right) \approx \langle a_{hp}^2 \rangle \frac{M_h}{M}. \quad (40)$$

We consider two phases for dynamical dark energy coupled to the halo structure formation and evolution in Eqs. (39) and (40). At a very high redshift when the total mass in haloes is negligible, $M_h/M \approx 0$ such that $\langle a_p^2 \rangle \approx \langle a_{op}^2 \rangle \propto a^{-1}$ (Fig. 4). In that situation, an exponent $\nu_0 = -1$ is required for a constant dark energy density in Eq. (39).

With the hierarchical formation of halo structures, the mass fraction $M_h/M \propto a^{1/2}$ increases with time and approaches one [49]. Since the acceleration fluctuations of out-of-halo particles are much smaller than that of halo particles ($\langle a_{op}^2 \rangle \ll \langle a_{hp}^2 \rangle$) in Fig. 4), we can make the approximation in Eq. (40) where acceleration fluctuations of halo particles become dominant over out-of-halo particles. With $\langle a_{hp}^2 \rangle \propto a^{-3/2}$ and $M_h \propto a^{1/2}$, an exponent $\nu_0 = -1$ is also required for a constant dark energy density in this phase.

Next, the acceleration fluctuations of halo particles read

$$\langle a_{hp}^2 \rangle = a_c^2 \approx a_{c0}^2 a^{-3/2}, \quad (41)$$

where $a_{c0} = a_c(z=0) \approx 10^{-10} m/s^2$ is the critical acceleration. The total mass of all haloes can be shown to follow a power-law scaling of $M_h \propto a^{1/2}$ in the matter era and reach a plateau in the dark energy era [43, 49, 50]. Therefore, the mass fraction of all haloes in all dark matter can be approximately modeled as

$$\frac{M_h}{M} = \alpha_h a^{1/2} (1 - \nu_a a)^{-1/2}, \quad (42)$$

where $\alpha_h \approx 0.6$ reflects that around 60% of all dark matter are in haloes at $z=0$ from N-body simulations. At small a , the scaling $M_h \propto a^{1/2}$ is recovered, while at large a , the mass fraction M_h/M levels off with a maximum mass fraction $\alpha_h (-\nu_a)^{-1/2}$ that is determined by the second parameter ν_a .

Putting all equations together, the dark energy density from acceleration fluctuations of the dark matter finally reads

$$\rho_{DE} = A_0 \frac{a_{c0}^2}{G} \alpha_h a^{-\nu_0-1} (1 - \nu_a a)^{-1/2},$$

or

$$\rho_{DE} = \rho_{DE0} a^{-\nu_0-1} \left(\frac{1 - \nu_a}{1 - \nu_a a} \right)^{1/2} \quad (43)$$

$$\text{where } \rho_{DE0} = A_0 \frac{a_{c0}^2}{G} \alpha_h (1 - \nu_a)^{-1/2}.$$

This is a double power-law evolution of dark energy density, i.e., $\rho_{DE} \propto a^{-\nu_0-1}$ in the matter era. With the total mass of all haloes M_h leveling off with time, the dark energy density decreases as $\rho_{DE} \propto a^{-\nu_0-3/2}$ in the dark energy era. The standard Λ CDM model with a constant dark energy density is recovered with $\nu_0 = -1$ and $\nu_a = 0$. With $\nu_0 = -1$, the model of Eq. (43) suggests a constant dark energy density phase in the matter era followed by a slowly decreasing phase of dark energy density as $\rho_{DE} \propto a^{-1/2}$. Here, ν_a is a shape parameter that determines the transition between two phases.

The proposed dark energy model involves two parameters ν_0 and ν_a (i.e., the $\nu_0\nu_a$ CDM model). Figure 21 presents the evolution of the $\nu_0\nu_a$ CDM model. When compared against the w_0w_a CDM model with constraints from DESI [66], the $\nu_0\nu_a$ CDM model has three distinct features: i) the evolution of dark energy is tightly coupled to the evolution of dark matter haloes; ii) model postulates that dark energy

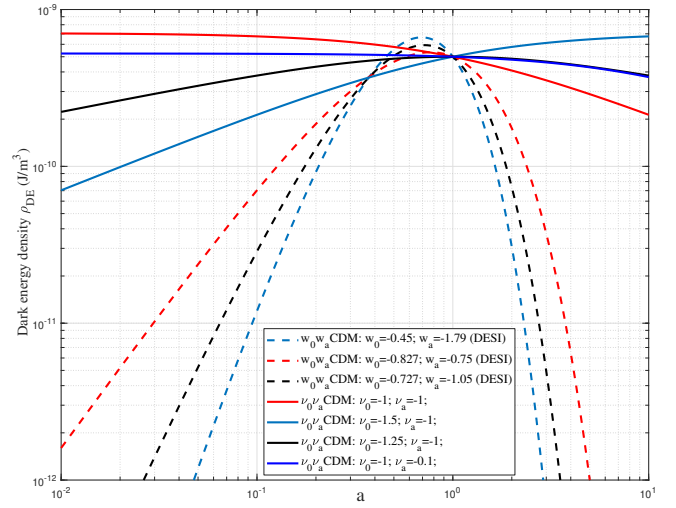


Figure 21. The evolution of dark energy density from the $\nu_0\nu_a$ CDM model (Eq. (43)) and from the w_0w_a CDM model (Eq. (36)). The $\nu_0\nu_a$ CDM model proposes the evolution of dark energy is tightly coupled to the evolution of dark matter haloes. The model postulates an entropic origin of dark energy from acceleration fluctuations of dark matter, which naturally gives rise to the dark energy density $\rho_{DE0} \approx a_{c0}^2/G = 10^{-10} \text{J/m}^3$. This model avoids the "cosmological constant problem" since dark energy is different from vacuum energy, the intrinsic energy of empty space. The model supports a dynamic evolution of dark energy with an almost constant dark energy density in the matter era, followed by a weakening dark energy when halo growth slows down. However, the $\nu_0\nu_a$ CDM model predicts a much slower power-law weakening compared to the exponential decrease in the w_0w_a CDM model.

originates from the acceleration fluctuations such that the "cosmological constant problem" can be avoided; iii) model suggests a constant dark energy density in the matter era and a weakening evolution in the dark energy era when structure formation slows down. However, the $\nu_0\nu_a$ CDM model predicts a much slower power-law weakening compared to the exponential decrease in the w_0w_a CDM model.

10 CONCLUSIONS

This paper focuses on the velocity and acceleration fluctuations in self-gravitating collisionless dark matter flow (SG-CFD) due to the long-range nature of gravity. Long-range interaction requires the formation of different sizes of haloes to maximize the entropy of the system [32]. These haloes facilitate an inverse mass and energy cascade from small to large scales with a constant rate of the energy cascade $\varepsilon_u \approx -10^{-7} m^2/s^3$ [50]. In addition to velocity fluctuations involving a critical velocity scale u_c , the long-range nature of gravity leads to fluctuations in acceleration with a critical scale a_c . The fluctuations in velocity and acceleration satisfy the relation $\varepsilon_u = -a_c u_c / (18\pi^2)$, which gives $a_c \approx 10^{-10} m/s^2$ for $u_c \approx 300 \text{km/s}$ at $z=0$. The critical acceleration scale a_c matches the empirical acceleration a_0 in the baryonic Tully-Fisher relation (BTFR) and the universal acceleration in MOND. In conventional wisdom, MOND is a competing empirical theory that potentially falsifies the dark matter hypothesis. Instead of falsifying dark matter, we suggest that MOND theory might be consistent with Λ CDM cosmology due to the velocity and acceleration fluctuations and the energy cascade in cold and collisionless dark matter. The "deep MOND" behavior can be recovered on the basis of this idea. More importantly, the predicted redshift dependence of $a_c \propto (1+z)^{3/4}$ is in good agreement with hydrodynamic simulations and observations. This redshift-dependent acceleration a_c

offers a powerful test to distinguish MOND and Λ CDM. In analogy to the kinetic pressure of gases that are produced by and proportional to velocity fluctuations, we postulate a similar "pressure" or "energy density" ρ_a that is induced by the acceleration fluctuations of dark matter. This energy density is proportional to acceleration fluctuations ($\rho_a \propto a_c^2/G$) and is of the order of 10^{-10} J/m³, or on the same order as the density of dark energy. Therefore, we postulate an entropic origin of the dark energy from the acceleration fluctuations, where the evolution of dark energy is coupled to the structure formation and evolution. A dynamical dark energy model ($\nu_0\nu_a$ CDM model in Eq. (43)) was proposed with a constant dark energy density at high redshift followed by a slow weakening phase.

ACKNOWLEDGMENTS

This research was supported by Laboratory Directed Research and Development at Pacific Northwest National Laboratory (PNNL). PNNL is a multiprogram national laboratory operated for the U.S. Department of Energy (DOE) by Battelle Memorial Institute under contract no. DE-AC05-76RL01830.

DATA AVAILABILITY

Two datasets underlying this article, i.e. halo-based and correlation-based dark matter flow statistics, are available on Zenodo [67, 68], along with the accompanying presentation slides 'A comparative study of dark matter flow & hydrodynamic turbulence and its applications' [69]. All data files are also available on GitHub [70].

References

- [1] V. C. Rubin and W. K. Ford, *Astrophysical Journal* **159**, 379 (1970).
- [2] V. C. Rubin, W. K. Ford, and N. Thonnard, *Astrophysical Journal* **238**, 471 (1980).
- [3] P. J. E. Peebles, *ApJ* **284**, 439 (1984).
- [4] D. N. Spergel, L. Verde, H. V. Peiris, E. Komatsu, M. R. Nolta, C. L. Bennett, M. Halpern, G. Hinshaw, N. Jarosik, A. Kogut, M. Limon, S. S. Meyer, L. Page, G. S. Tucker, J. L. Weiland, E. Wollack, and E. L. Wright, *The Astrophysical Journal Supplement Series* **148**, 175 (2003), arXiv:astro-ph/0302209 [astro-ph].
- [5] E. Komatsu, K. M. Smith, J. Dunkley, C. L. Bennett, B. Gold, G. Hinshaw, N. Jarosik, D. Larson, M. R. Nolta, L. Page, D. N. Spergel, M. Halpern, R. S. Hill, A. Kogut, M. Limon, S. S. Meyer, N. Odegard, G. S. Tucker, J. L. Weiland, E. Wollack, and E. L. Wright, *The Astrophysical Journal Supplement Series* **192**, 18 (2011), arXiv:1001.4538 [astro-ph.CO].
- [6] C. S. Frenk and S. D. M. White, *Annalen der Physik* **524**, 507 (2012), arXiv:1210.0544 [astro-ph.CO].
- [7] J. S. Bullock and M. Boylan-Kolchin, *ARA&A* **55**, 343 (2017), arXiv:1707.04256 [astro-ph.CO].
- [8] A. Del Popolo and M. Le Delliou, *Galaxies* **5**, 17 (2017), arXiv:1606.07790 [astro-ph.CO].
- [9] L. Perivolaropoulos and F. Skara, *New Astronomy Reviews* **95**, 101659 (2022).
- [10] R. A. Flores and J. R. Primack, *ApJ* **427**, L1 (1994), arXiv:astro-ph/9402004 [astro-ph].
- [11] B. Moore, *nat* **370**, 629 (1994).
- [12] W. J. G. de Blok, *Adv. Astron.* **2010**, 789293 (2010), arXiv:0910.3538 [astro-ph.CO].
- [13] A. Klypin, A. V. Kravtsov, O. Valenzuela, and F. Prada, *The Astrophysical Journal* **522**, 82 (1999).
- [14] B. Moore, S. Ghigna, F. Governato, G. Lake, T. Quinn, J. Stadel, and P. Tozzi, *The Astrophysical Journal* **524**, L19 (1999).
- [15] M. Boylan-Kolchin, J. S. Bullock, and M. Kaplinghat, *Monthly Notices of the Royal Astronomical Society: Letters* **415**, L40 (2011).
- [16] M. Boylan-Kolchin, J. S. Bullock, and M. Kaplinghat, *Monthly Notices of the Royal Astronomical Society* **422**, 1203 (2012), <https://academic.oup.com/mnras/article-pdf/422/2/1203/3464467/mnras0422-1203.pdf>.
- [17] R. B. Tully and J. R. Fisher, *Astronomy & Astrophysics* **54**, 661 (1977).
- [18] S. M. Faber and R. E. Jackson, *Astrophysical Journal* **204**, 668 (1976).
- [19] S. S. McGaugh, J. M. Schombert, G. D. Bothun, and W. J. G. de Blok, *Astrophysical Journal* **533**, L99 (2000).
- [20] E. F. Bell and R. S. de Jong, *ApJ* **550**, 212 (2001), arXiv:astro-ph/0011493 [astro-ph].
- [21] M. A. W. Verheijen, *The Astrophysical Journal* **563**, 694 (2001).
- [22] C. Wheeler, P. F. Hopkins, and O. Doré, *ApJ* **882**, 46 (2019), arXiv:1803.01849 [astro-ph.GA].
- [23] A. A. Dutton, *Monthly Notices of the Royal Astronomical Society* **424**, 3123 (2012), <https://academic.oup.com/mnras/article-pdf/424/4/3123/18715174/424-4-3123.pdf>.
- [24] B. Famaey and S. McGaugh, in *Journal of Physics Conference Series*, Journal of Physics Conference Series, Vol. 437 (2013) p. 012001, arXiv:1301.0623 [astro-ph.CO].
- [25] M. Milgrom, *Astrophysical Journal* **270**, 365 (1983).
- [26] S. S. McGaugh and W. J. G. de Blok, *Astrophysical Journal* **499**, 41 (1998).
- [27] F. Lelli, S. S. McGaugh, J. M. Schombert, H. Desmond, and H. Katz, *Monthly Notices of the Royal Astronomical Society* **484**, 3267 (2019).
- [28] S. S. McGaugh, F. Lelli, and J. M. Schombert, *Physical Review Letters* **117** (2016), 10.1103/physrevlett.117.201101.
- [29] B. W. Keller and J. W. Wadsley, *The Astrophysical Journal Letters* **835**, L17 (2017), arXiv:1610.06183 [astro-ph.GA].
- [30] K. M. Gorski, M. Davis, M. A. Strauss, S. D. M. White, and A. Yahil, *Astrophysical Journal* **344**, 1 (1989).
- [31] O. Hahn, R. E. Angulo, and T. Abel, *Monthly Notices of the Royal Astronomical Society* **454**, 3920 (2015).
- [32] Z. Xu, *A&A* **675**, A92 (2023), arXiv:2110.03126 [astro-ph].
- [33] Z. Xu, *Physics of Fluids* **35**, 077105 (2023), arXiv:2202.00910 [astro-ph].
- [34] Z. Xu, *Physics of Fluids* **36**, 117158 (2024), arXiv:2202.06515 [astro-ph].
- [35] Z. Xu, *Physics of Fluids* **36**, 075146 (2024), arXiv:2202.02991 [astro-ph].
- [36] H. Mo, F. van den Bosch, and S. White, *Galaxy formation and evolution* (Cambridge University Press, Cambridge, 2010).
- [37] P. J. E. Peebles, *The Large-Scale Structure of the Universe* (Princeton University Press, Princeton, NJ, 1980).
- [38] C. S. Frenk, J. M. Colberg, H. M. P. Couchman, G. Efstathiou, A. E. Evrard, A. Jenkins, T. J. MacFarland, B. Moore, J. A. Peacock, F. R. Pearce, P. A. Thomas, S. D. M. White, and N. Yoshida., arXiv:astro-ph/0007362v1 (2000),

- 10.48550/arXiv.astro-ph/0007362.
- [39] A. Jenkins, C. S. Frenk, F. R. Pearce, P. A. Thomas, J. M. Colberg, S. D. M. White, H. M. P. Couchman, J. A. Peacock, G. Efstathiou, and A. H. Nelson, *Astrophysical Journal* **499**, 20 (1998).
- [40] J. M. Colberg, S. D. M. White, A. Jenkins, and F. R. Pearce, *Monthly Notices of the Royal Astronomical Society* **308**, 593 (1999).
- [41] R. K. Sheth, H. J. Mo, and G. Tormen, *Monthly Notices of the Royal Astronomical Society* **323**, 1 (2001).
- [42] D. Nelson, A. Pillepich, S. Genel, M. Vogelsberger, V. Springel, P. Torrey, V. Rodriguez-Gomez, D. Sijacki, G. Snyder, B. Griffen, F. Marinacci, L. Blecha, L. Sales, D. Xu, and L. Hernquist, *Astronomy and Computing* **13**, 12 (2015).
- [43] Z. Xu, *arXiv e-prints*, arXiv:2202.07240 (2022).
- [44] Z. Xu, *Monthly Notices of the Royal Astronomical Society* **536**, 3554 (2024), arXiv:2501.07608 [astro-ph] .
- [45] E. T. Jaynes, *Physical Review* **106**, 620 (1957).
- [46] E. T. Jaynes, *Physical Review* **108**, 171 (1957).
- [47] A. Cooray and R. Sheth, *Physics Reports-Review Section of Physics Letters* **372**, 1 (2002).
- [48] Z. Xu, *Scientific Reports* **13**, 4165 (2023), arXiv:2209.03313 [astro-ph] .
- [49] Z. Xu, *Scientific Reports* **13**, 16531 (2023), arXiv:2210.01200 [astro-ph] .
- [50] Z. Xu, *arXiv e-prints*, arXiv:2109.09985 (2021).
- [51] Z. Xu, *arXiv e-prints*, arXiv:2110.05784 (2021).
- [52] Y. B. Zeldovich, *Astronomy & Astrophysics* **5**, 84 (1970).
- [53] J. E. Gunn, *Astrophysical Journal* **218**, 592 (1977).
- [54] G. I. Taylor, *Proceedings of the Royal Society of London Series a-Mathematical and Physical Sciences* **164**, 0015 (1938).
- [55] A. C. Mayer, A. F. Teklu, K. Dolag, and R.-S. Remus, *Monthly Notices of the Royal Astronomical Society* **518**, 257 (2022), <https://academic.oup.com/mnras/article-pdf/518/1/257/4704252/stac3017.pdf> .
- [56] D.-C. Dai and C. Lu, *Phys. Rev. D* **96**, 124016 (2017).
- [57] M. Milgrom, *Acta Physica Polonica B* **32**, 3613 (2001).
- [58] D. Obreschkow, D. Croton, G. De Lucia, S. Khochfar, and S. Rawlings, *The Astrophysical Journal* **698**, 1467 (2009).
- [59] G. Sharma, V. Upadhyaya, P. Salucci, and S. Desai, *A&A* **689**, A318 (2024), arXiv:2406.08934 [astro-ph.GA] .
- [60] H. Übler, N. M. Förster Schreiber, R. Genzel, E. Wisnioski, S. Wuyts, P. Lang, T. Naab, A. Burkert, P. G. van Dokkum, L. J. Tacconi, D. J. Wilman, M. Fossati, J. T. Mendel, A. Beifiori, S. Belli, R. Bender, G. B. Brammer, J. Chan, R. Davies, M. Fabricius, A. Galametz, D. Lutz, I. G. Momcheva, E. J. Nelson, R. P. Saglia, S. Seitz, and K. Tadaki, *The Astrophysical Journal* **842**, 121 (2017).
- [61] C. M. S. Straatman, K. Glazebrook, G. G. Kacprzak, I. Labbé, T. Nanayakkara, L. Alcorn, M. Cowley, L. J. Kewley, L. R. Spitler, K.-V. H. Tran, and T. Yuan, *The Astrophysical Journal* **839**, 57 (2017).
- [62] F. Lelli, S. S. McGaugh, and J. M. Schombert, *The Astrophysical Journal Letters* **816**, L14 (2016).
- [63] J. E. Gunn and J. R. Gott, *Astrophysical Journal* **176**, 1 (1972).
- [64] S. N. Gurbatov, A. I. Saichev, and S. F. Shandarin, *Monthly Notices of the Royal Astronomical Society* **236**, 385 (1989).
- [65] A. Tripathi, A. Sangwan, and H. Jassal, *Journal of Cosmology and Astroparticle Physics* **2017**, 012 (2017).
- [66] A. G. Adame, J. Aguilar, S. Ahlen, S. Alam, D. M. Alexander, M. Alvarez, O. Alves, A. Anand, U. Andrade, E. Armengaud, S. Avila, A. Aviles, H. Awan, B. Bahr-Kalus, S. Bailey, C. Baltay, A. Bault, J. Behera, S. BenZvi, A. Bera, F. Beutler, D. Bianchi, C. Blake, R. Blum, S. Brieden, A. Brodzeller, D. Brooks, E. Buckley-Geer, E. Burtin, R. Calderon, R. Canning, A. C. Rosell, R. Cereskaite, J. L. Cervantes-Cota, S. Chabanier, E. Chaussidon, J. Chaves-Montero, S. Chen, X. Chen, T. Claybaugh, S. Cole, A. Cuceu, T. M. Davis, K. Dawson, A. de la Macorra, A. de Mattia, N. Deiosso, A. Dey, B. Dey, Z. Ding, P. Doel, J. Edelman, S. Eftekharzadeh, D. J. Eisenstein, A. Elliott, P. Fagrellius, K. Fanning, S. Ferraro, J. Ereza, N. Findlay, B. Flaugher, A. Font-Ribera, D. Forero-Sánchez, J. E. Forero-Romero, C. S. Frenk, C. Garcia-Quintero, E. Gaztañaga, H. Gil-Marín, S. G. A. Gontcho, A. X. Gonzalez-Morales, V. Gonzalez-Perez, C. Gordon, D. Green, D. Gruen, R. Gspaner, G. Gutierrez, J. Guy, B. Hadzhiyska, C. Hahn, M. M. S. Hanif, H. K. Herrera-Alcantar, K. Honscheid, C. Howlett, D. Huterer, V. Iršič, M. Ishak, S. Juneau, N. G. Karaçaylı, R. Kehoe, S. Kent, D. Kirkby, A. Kremin, A. Krolewski, Y. Lai, T. W. Lan, M. Landriau, D. Lang, J. Lasker, J. M. L. Goff, L. L. Guillou, A. Leauthaud, M. E. Levi, T. S. Li, E. Linder, K. Lodha, C. Magneville, M. Manera, D. Margala, P. Martini, M. Maus, P. McDonald, L. Medina-Varela, A. Meisner, J. Mena-Fernández, R. Miquel, J. Moon, S. Moore, J. Moustakas, N. Mudur, E. Mueller, A. Muñoz-Gutiérrez, A. D. Myers, S. Nadathur, L. Napolitano, R. Neveux, J. A. Newman, N. M. Nguyen, J. Nie, G. Niz, H. E. Noriega, N. Padmanabhan, E. Paillas, N. Palanque-Delabrouille, J. Pan, S. Penmetsa, W. J. Percival, M. M. Pieri, M. Pinon, C. Poppett, A. Porredon, F. Prada, A. Pérez-Fernández, I. Pérez-Ràfols, D. Rabbinowitz, A. Raichoor, C. Ramírez-Pérez, S. Ramirez-Solano, C. Ravoux, M. Rashkovetskyi, M. Rezaie, J. Rich, A. Rocher, C. Rockosi, N. A. Roe, A. Rosado-Marin, A. J. Ross, G. Rossi, R. Ruggeri, V. Ruhlmann-Kleider, L. Samushia, E. Sanchez, C. Saulder, E. F. Schlafly, D. Schlegel, M. Schubnell, H. Seo, A. Shafieloo, R. Sharples, J. Silber, A. Slosar, A. Smith, D. Sprayberry, T. Tan, G. Tarlé, P. Taylor, S. Trusov, L. A. Ureña-López, R. Vaisakh, D. Valcin, F. Valdes, M. Vargas-Magaña, L. Verde, M. Walthers, B. Wang, M. S. Wang, B. A. Weaver, N. Weaverdyck, R. H. Wechsler, D. H. Weinberg, M. White, J. Yu, Y. Yu, S. Yuan, C. Yèche, E. A. Zaborowski, P. Zarrouk, H. Zhang, C. Zhao, R. Zhao, R. Zhou, T. Zhuang, and H. Zou, “Desi 2024 vi: Cosmological constraints from the measurements of baryon acoustic oscillations,” (2024), arXiv:2404.03002 [astro-ph.CO] .
- [67] Z. Xu, “Dark matter flow dataset part i: Halo-based statistics from cosmological n-body simulation,” (2022).
- [68] Z. Xu, “Dark matter flow dataset part ii: Correlation-based statistics from cosmological n-body simulation,” (2022).
- [69] Z. Xu, “A comparative study of dark matter flow & hydrodynamic turbulence and its applications,” (2022).
- [70] Z. Xu, “Dark matter flow dataset,” (2022).